

Abstract

This thesis investigates superconductivity in system with flat electronic bands, which support high T_C superconductivity.

With a particular focus on the coherence length (describing the size of Cooper pairs) and the London penetration depth (describing the distance magnetic fields can penetrate into the material). These length scales are connected to the properties of the material when in the superconducting state.

The method to calculate the superconducting length scales works by extracting information on the length scales from the breakdown of the order parameter when introducing a finite momentum.

A class of systems attracting significant recent interest are graphene based system that host flat band due to specific structural configurations. The model investigated in this thesis is a conceptually simple model of a flat band hybridized with graphene that can be realized in two-dimensional adatom hetero structures.

The finite-momentum pairing method is applied to both this decorated graphene model and a one-band Hubbard model with a simple local attractive interaction. The superconducting length scales are calculated and compared between the Bardeen-Cooper-Schrieffer (BCS) and Dynamical Mean Field Theory (DMFT) frameworks.

Kurzzusammenfassung

[Check translation](#)

Diese Arbeit untersucht Supraleitung mit einem besonderen Fokus auf die Kohärenzlänge (die die Ausdehnung von Cooper-Paaren beschreibt) und die London'sche Eindringtiefe (die angibt, wie weit Magnetfelder in ein Material eindringen können). Diese Längenskalen sind eng mit den Materialeigenschaften im supraleitenden Zustand verknüpft.

Die Methode basiert auf der Ginzburg-Landau-Theorie, wobei dem Ordnungsparameter ein endlicher Impuls zugewiesen wird. Um diese Längenskalen in mikroskopischen Theorien zu berechnen, muss dieser endliche Impuls in das jeweilige theoretische Rahmenwerk eingeführt werden. In der theoretischen Einleitung wird dieser Zugang sowohl in Bardeen-Cooper-Schrieffer (BCS)-Theorie als auch in Dynamische Molekularfeld-Theorie demonstriert.

In jüngster Zeit haben Systeme mit flachen elektronischen Bändern an Bedeutung gewonnen, insbesondere Graphen-basierte Systeme, in denen flache Bänder aufgrund spezieller struktureller Eigenschaften auftreten. Ein in dieser Arbeit behandeltes Beispiel besteht aus einer Schicht von Gruppe-IV-Atomen zwischen einer Graphenlage und einem SiC-Substrat. Ein Minimalmodell für dieses System ist eine modifizierte Graphenstruktur mit einem zusätzlichen Atom in der Einheitszelle, das das flache Band stellt.

Die Methode der Paarbildung mit endlichem Impuls wird sowohl auf dieses dekorierte Graphenmodell als auch auf ein Ein-Band-Hubbard-Modell mit einer einfachen lokalen attraktiven Wechselwirkung angewendet. Die supraleitenden Längenskalen werden berechnet und zwischen den BCS- und Dynamical Mean Field Theory (DMFT)-Ansätzen verglichen.

Die Arbeit schließt mit einer Diskussion über mögliche Anwendungen der Methode auf realistischere Versionen des dekorierten Graphenmodells sowie über die Perspektiven einer vollständigen DMFT-Behandlung in diesem Kontext.

Contents

1	Introduction	1
2	Superconductivity	8
2.1	Ginzburg-Landau Theory of Superconductivity	9
2.2	Bardeen-Cooper-Schrieffer Theory	17
2.3	Dynamical Mean-Field Theory	23
2.4	Quantum Geometry	30
3	Decorated Graphene Model	36
3.1	Lattice Structure	37
3.2	Quantum Geometry	41
4	Application of the Finite-Momentum Pairing Method	43
4.1	BCS: Decorated graphene Model	43
4.2	BCS and DMFT: One-Band Hubbard Model on the Square Lattice	53
5	Conclusion	55
	Bibliography	58
	Not cited	66
	Listings	69
	List of Figures	69
	List of Acronyms	70

Todo list

Check translation	ii
Word that better	8
Mean field expression for Hubbard int	19
Make notation coherent with my BCS notation for non-interacting H . . .	33
Talk about limitation of GL: does not apply for high q	47
Make that properly	49
Talk about the exact moment of the switchover	50
Talk about London penetration depth	50
Where is the maximum of q_m , compared with maximum of Aalto DS . .	52
Is that correct?	52
Talk about the fact that the method works for all U values	53
Minimal value of coherence length?	53
Write what goes on in the high U limit between MF and DMFT	54
Why? What is captured in DMFT?	54
Split up figure	56

1

Introduction

The United Nations declared 2025 the ‘International Year of Quantum Science and Technology’ [1]. This is an effort is to raise awareness of the importance of quantum science and its applications, which focuses in 3 key areas: quantum computing, quantum communications and quantum sensors.

One effect underlying many of these applications is the phenomenon of superconductivity, a phase of matter characterized by vanishing electrical resistance and expulsion of magnetic field. For example, superconducting qubits are a promising platform for scalable quantum computing [2, 3] and the Josephson effect [4] can be used to build extremely sensitive measurement devices for magnetic fields [5] or voltages [6].

Superconductivity

Superconductivity was discovered in 1911, when Heike Onnes measured that the electrical resistance of Mercury vanished completely when cooling it below 4 K [7]. In the following decades, more properties in superconducting materials were discovered such as the Meissner effect, the perfect expulsion of magnetic fields [8]. The phenomenological theory by London described the superconducting as a single wave function [9] which explained the Meissner effect. In 1957, Bardeen, Cooper and Schrieffer published their theory of superconductivity [10], which describes it as the result of condensation of electrons into (so called Cooper-)pairs via an phonon-mediated attractive interaction. This condensate plays the role of the wave function in the London theory and thus explained the Meissner effect from a microscopic theory.

Based on Bardeen-Cooper-Schrieffer (BCS) theory, Cohen and Anderson derived a maximal T_C of 30 K [11], which was broken in 1986 by the discovery of superconductivity in cuprates [12, 13]. Since then, many different families of superconductors have been discovered. Commonly, superconducting materials are characterized along four dimensions [14]:

- **conventional/unconventional:** there are different concrete definition that capture essentially the same thing, most commonly ‘conventional’ super-

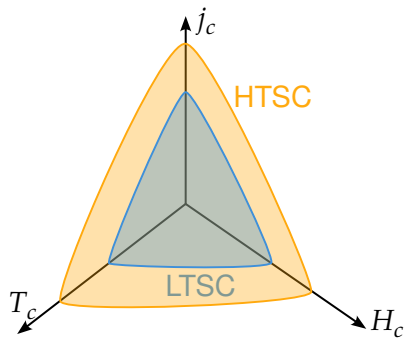


Figure 1.1 – Critical surface of a superconductor. For practical applications, this surface is desired to be as large as possible, making it possible to carry high currents and generate strong magnetic fields while not needing to cool the superconductor to very low temperatures. This generally is the case for high-temperature superconductors (HTSC) in comparison to low-temperature superconductors (LTSC).

conductors are materials that can be described by the phonon mediated attraction in BCS theory

- **low/high temperature:** while the Cuprates were the first high temperature superconductors, today the boiling point of liquid nitrogen (77K) is set as the separation between low and high temperature superconductors.
- **weak/strong coupling:** in the context of superconductivity, coupling strength refers to the strength of the interaction driving the pair condensation. Independent of the specific mechanism, the coupling strength is used to characterize the spatial extent of the electron pairs.
- **weakly/strongly correlated:** the correlation strength describes how strong the influence electron-electron interactions are in comparison to the kinetic energy. Similarly to the coupling strength, stronger electron-electron interactions are associated with electron localization.

High temperature superconductors not only have higher T_C so that lower-cost cooling methods can be employed, they typically also support stronger currents and can withstand higher magnetic fields until the superconducting order breaks down. These three parameters span the critical surface (see fig. 1.1).

The critical field and critical current are deeply connected to two intrinsic length scales of superconductors: coherence length ξ_0 and the London penetration depth $\lambda_{L,0}$. They are accessible in BCS theory, but inaccessible in the presence of strong electronic correlations.

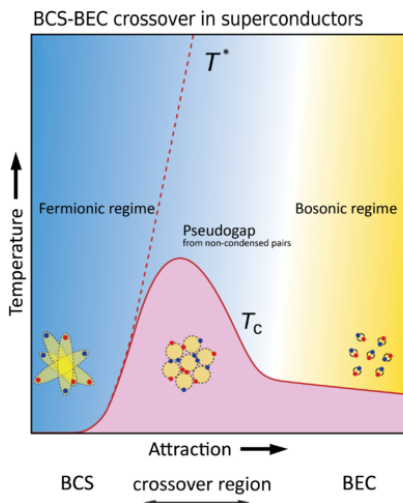


Figure 1.2 – BCS-BEC crossover. This is a general illustration of the crossover between loosely bound (BCS regime) and tightly bound (BEC regime) pairs in superconductors. The crossover begins at the point where the pair creation temperature T^* diverges from the superconducting transition temperature T_C , at which the pairs condense. Reprinted figure with permission from [15]. Copyright 2024 by the American Physical Society.

BCS-BEC Crossover

One topic emerging in the context of high T_C superconductors is the description in the BCS-BEC crossover [15]. It is a framework independent of the specific pairing mechanism and characterizes superconductivity on the axis of weak to strong coupling. Figure 1.2 shows the two regimes that can be connected by tuning the generalized coupling: the BCS regime with large electron pairs and the Bose-Einstein condensate regime with tightly bound pairs. The T_C in fig. 1.2 has a dome-shape going from the weak to strong pairing, which is reminiscent of the dome shape against doping in many unconventional superconductors such as the Cuprates as well as the pseudogap parent state.

The intermediate region is characterized by the fact that despite the electron pairing up (marked by T^*), there is no superconductivity. This is due to the fact that besides pairing, also phase coherence is needed for superconducting order which is suppressed when the stronger attraction impairs pair mobility. The BCS-BEC crossover phenomenology gives qualitative insights in what limits T_C , which is again strongly connected to the superconducting length scales: in the BCS regime, the energy scale that limits T_C is the pairing energy Δ which is related to the coherence length ξ_0 while in the BEC regime it is the phase coherence energy D_S , which is directly related to the London penetration depth $\lambda_{L,0}$ via $D_S = \lambda_{L,0}^{-2}$. This gives a possible route to raising T_C by evading the constraints of the BCS-BEC crossover in the strong-coupling regime [16, 17].

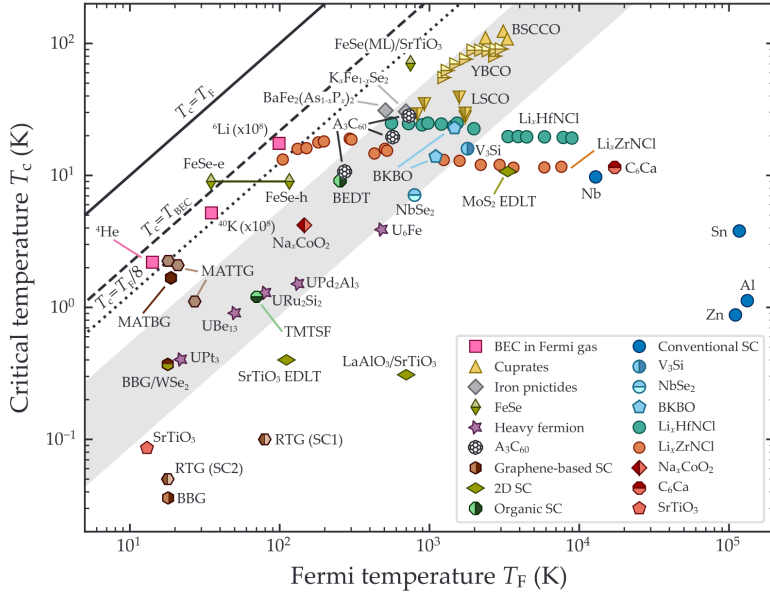


Figure 1.3 – Uemura plot. Comparison of Fermi temperature T_F and critical temperature T_C for various families of superconductors on a logarithmic plot. The gray shaded region marks the regime where most unconventional superconductors are located (here $T_C = 0.04T_{BEC}$ to $T_C = 0.25T_{BEC}$). The lines marks different limits for T_C : the solid line being $T_C = T_F$, the dashed line is the critical temperature of a non-interacting BEC ($T_{BEC} = T_F/4.16$) and the upper limit for the Berezinskii–Kosterlitz–Thouless transition of free electrons in two dimensions $T_C = T_F/8$ as a dotted line. Taken from [14] with data from [19–21].

This is explored for the example of Alkali-doped fullerides in ref. [18]: by exploiting the high degrees of freedom in this multi-orbital system, the typical constraint on the superfluid stiffness imposed by the lattice can be evaded, enabling high T_C in this regime.

Strong Correlations in Graphene Based Systems

Graphene, the two-dimensional allotrope of Carbon was first synthesized in 2004 [22]. It sparked the field of 2D materials, which shows unique properties due to the confinement in one dimension and extensive tunability with environ-

mental dielectric screening, electrostatic doping or tuning with external fields [23].

Over time, another tuning parameter emerged: it turned out that two graphene layer twisted against each other as seen in fig. 1.4a host localized electrons with pronounced interaction effects for certain twist angles. In 2018, Cao et al. measured superconductivity in this setup with a phase diagram very similar to the Cuprates [24]. Another method to enhance interaction effects in graphene based systems are multilayer systems without twisting, such as Bernal bilayer, ABC or ABCA layered systems [25].

Especially in these flat band systems exhibiting superconductivity, the geometry of the space spanned by the electronic Bloch states (the so-called quantum geometry) is crucial for stabilizing the superconducting state. This is due to the fact that for a single band, the superfluid weight is given by the curvature of the band, so zero in the flat band case. In multiband systems, the quantum geometry gives a contribution that can be non-zero even for flat-band systems [26].

For the graphene systems discussed above, the strong quantum geometry comes from the graphene Dirac cones [27], playing a role in stabilizing superconducting [26, 28, 29] and magnetic order [30, 31] in the multilayer systems.

In the Uemura plot fig. 1.3, twisted Bilayer and Trilayer graphene are very close to the theoretical 2D limit and they lie outside the line of most unconventional superconductors. This makes them very ‘efficient’: they show a high T_C for their low Fermi temperature/carrier density, so further efforts in the class of graphene based flat band systems might lead to key insights into superconductivity with even higher T_C .

Organization of this thesis

The graphene structures discussed above are an interesting class for novel superconductors in itself and the insight gained from them informs many other avenues to better superconducting materials. In light of this, the goal of this thesis is to develop Finite Momentum Pairing (FMP) method in BCS theory, apply it to a flat band model in decorated graphene and then compared to application of the Dynamical Mean Field Theory (DMFT) method on the one band Hubbard model.

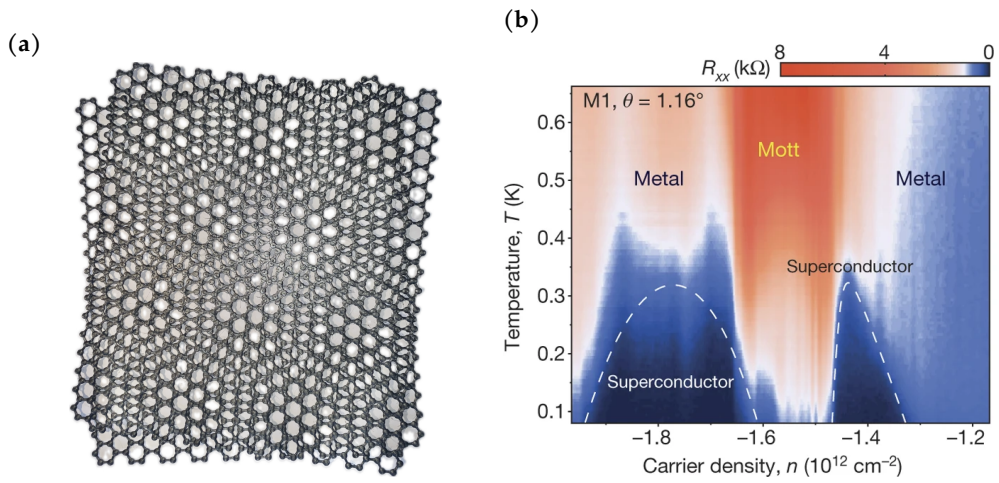


Figure 1.4 – Twisted Bilayer graphene. (a) Moiré pattern formed by imposing two hexagonal lattices on top of each other with a twist angle. The emerging pattern has brighter regions where the layer approximately align and darker regions where the top-layer atoms in the A sublattice sit roughly above the B atoms in the bottom layer, but the top-layer B atoms have no partner in the bottom layer. (b) Phase diagram of the twisted Bilayer graphene showing the dependence of T_C on the carrier density in the partially filled flat band. Reproduced from [24] with permission from Springer Nature.

Chapter 2 reviews aspects of the theoretical description of superconductors, in particular the Ginzburg-Landau theory which is the foundation for the FMP method. Furthermore, BCS theory and DMFT under the FMP constraint are explained. The decorated graphene model and its experimental basis are reviewed in chapter 3. The FMP method is then applied in chapter 4, in the BCS formulation for the decorated graphene model and in the DMFT formulation for the simpler one band Hubbard model on the square lattice. In the last chapter (chapter 5), further pathways for investigation using the tools discussed in the thesis are presented.

2

Superconductivity

Superconductivity research has been pushing our understanding of quantum and material science [32]. In this chapter I will review the concepts necessary for understanding superconductivity and introduce the tools used to study it in the later chapters. There are many textbooks covering these topics which can be referenced for a more detailed treatment, such as refs. [33–37].

The superconducting state is a condensation of electrons into pairs with a macroscopically coherent phase, which spontaneously breaks the $U(1)$ phase rotation symmetry. This fixed phase leads to superfluidity in neutral atoms like H_4 or cold atomic gases and superconductivity in superconductors, which can both be phenomenologically explained in Ginzburg-Landau theory, discussed in section 2.1. Both phenomena are characterized by dissipationless flow, of neutral atoms in one case and charged electron pairs in the other. For this reason, similar nomenclature is used, for example the current in a superconductor is often called a charged superflow.

Ginzburg-Landau theory introduces two length scales inherent to superconductors: the coherence length ξ_0 describing the length scale of amplitude variations of the order parameter and the London penetration depth λ_L , which is connected to energy cost of phase variations of the order parameter. They also connect to the energy gap Δ and the condensate stiffness D_S , which are often competing energy scales in superconductors [16, 17].

The interplay of these length (energy) scales determine the macroscopic properties of a superconductors, so there is a great interest in accessing them from microscopic theories. To this end, section 2.1 also introduces a theoretical framework based on Cooper pairs with finite momentum [18] that will be used in later chapters to calculate these length scales from microscopic theories. Two of these microscopic theories, BCS theory and DMFT will be introduced in section 2.2 and section 2.3 respectively.

Furthermore, section 2.4 introduces an emerging perspective in the study of novel superconductors: it turns out that the superfluid weight is connected to a property of the electronic band structure called the quantum metric [26, 38].

Word that
better

2.1 Ginzburg-Landau Theory of Superconductivity

Spontaneous Symmetry Breaking and Order Parameter

Symmetries are a powerful concept in physics as for example Noethers theorem [39] connects the symmetries of physical theories to associated conservation laws.

An interesting facet of symmetries in physical theories is the fact that a ground state of a system must not necessarily obey the same symmetries as its Hamiltonian. So for a symmetry operation that is described by a unitary operator U , the Hamiltonian commutes with U , which results in expectation values of the Hamiltonian being invariant under the symmetry operation, but the states $|\phi\rangle$ and $U|\phi\rangle$ can be different. This phenomenon is called spontaneous symmetry breaking and the state $|\phi\rangle$ is said to be symmetry-broken [40]. One consequence of this fact is that for a given symmetry-broken state $|\phi\rangle$, there exist multiple states with the same energy that can be reached by repeatedly applying U to $|\phi\rangle$. The symmetry-broken states can be differentiated by an operator that has a finite expectation value Ψ below the transition temperature T_C :

$$|\Psi| = \begin{cases} 0 & T \geq T_C \\ |\Psi_0| > 0 & T < T_C \end{cases}. \quad (2.1)$$

Generally, Ψ can be a complex-valued vector and is called the order parameter. In the example of a ferromagnet, a finite magnetization of a material is associated with a finite expectation value for the z -component of the spin operator, $m_z = \langle \hat{S}_z \rangle$.

Similarly to a magnetically ordered state, the superconducting state is characterized by an order parameter. The theory of phase transitions in superconductors was developed by Ginzburg and Landau [41]. Landau theory and conversely Ginzburg-Landau theory is not concerned with the microscopic properties of the order parameter, but describes the changes in thermodynamic properties of matter when the order parameter assumes a finite value. In the context of superconductivity, the order parameter is a complex quantity

$$\Psi = \Psi_1 + i\Psi_2 = |\Psi|e^{i\phi}. \quad (2.2)$$

and is connected to the pairing amplitude

$$\Delta_{\mathbf{k}} = - \sum_{\mathbf{k}'} V_{\mathbf{k},\mathbf{k}'} \langle c_{-\mathbf{k}'\downarrow} c_{\mathbf{k}'\uparrow} \rangle, \quad (2.3)$$

i.e. the expectation value for the coherent creation of electron pairs of opposite momentum and spin.

Landau and Ginzburg-Landau Theory

Underlying Landau theory is the concept of the free energy: it is a thermodynamic potential as a function of state variables that is minimized in thermodynamic equilibrium. The fundamental idea of Landau theory is now to write the free energy $F[\Psi]$ as function of the order parameter Ψ and expand it as a polynomial:

$$F_L[\Psi] = \int d^d x f_L[\Psi], \quad (2.4)$$

where

$$f_L[\Psi] = \frac{r}{2}\Psi^2 + \frac{u}{4}\Psi^4 \quad (2.5)$$

is called the free energy density. The stationary point of f_L can be found from the condition

$$\frac{\delta f_L}{\delta \Psi} = r\Psi + u\Psi^3 \stackrel{!}{=} 0 \quad (2.6)$$

which gives

$$\Psi = 0 \vee \Psi = \pm \sqrt{\frac{r}{u}} \quad (2.7)$$

For a stable systems $r > 0$ is required, so for the order parameter to assume a finite value at a critical temperature T_C , the parameter r needs to change sign:

$$r = a(T - T_C). \quad (2.8)$$

Figure 2.1a shows the free energy as a function of a single-component, real order parameter Ψ . From the temperature dependence of the order parameter, the critical temperature T_C can be extracted from the behavior of the order parameter near T_C via a linear fit of

$$|\Psi|^2 \propto T_C - T. \quad (2.9)$$

The Landau free energy for a complex order parameter takes the form

$$f_L[\Psi] = r\Psi^*\Psi + \frac{u}{2}(\Psi^*\Psi)^2 = r|\Psi|^2 + \frac{u}{2}|\Psi|^4 \quad (2.10)$$

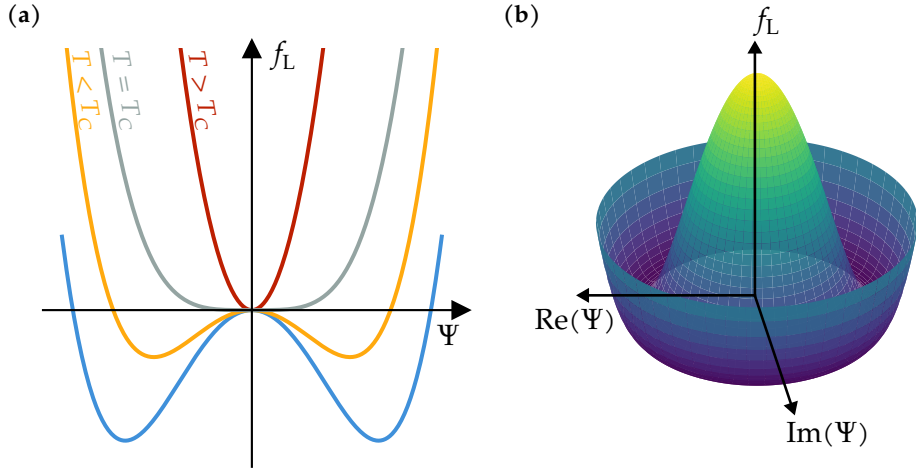


Figure 2.1 – Landau free energy and Mexican hat potential. (a) Landau free energy f_L for a real-valued order parameter Ψ at different temperatures T . (b) Landau free energy for a complex order parameter Ψ .

with again

$$r = a(T_C - T) . \quad (2.11)$$

Instead of the two minima, the free energy here has rotation symmetry, since it is independent of the phase of the order parameter:

$$f_L[\Psi] = f_L[e^{i\phi}\Psi] . \quad (2.12)$$

This results in the so called ‘Mexican hat’ potential shown in fig. 2.1b. In this potential, the phase of the order parameter can be rotated continuously, so that there is actually a continuum of symmetry-broken states.

In 1950, V. L. Ginzburg and L.D. Landau published their theory of superconductivity, based on Landau’s theory of phase transitions [41]. Where Landau theory as described above has a uniform order parameter, Ginzburg-Landau theory accounts for it being spatially inhomogeneous. The free energy has an additional gradient term $\nabla\Psi$ in comparison to the Landau free energy:

$$f_{\text{GL}}[\Psi, \nabla\Psi] = \frac{\hbar^2}{2m^*} |\nabla\Psi|^2 + r|\Psi|^2 + \frac{u}{2} |\Psi|^4 , \quad (2.13)$$

It is sensitive to a twist of the phase of the order parameter: Writing $\Psi = |\Psi|e^{i\phi}$, the gradient term is

$$\Delta\Psi = (\nabla|\Psi| + i\nabla\phi|\Psi|)e^{i\phi}. \quad (2.14)$$

With that, eq. (2.13) becomes

$$f_{GL} = \frac{\hbar^2}{2m^*}|\Psi|^2(\nabla\phi)^2 + \left[\frac{\hbar^2}{2m^*}(\nabla|\Psi|)^2 + r|\Psi|^2 + \frac{u}{2}|\Psi|^4 \right]. \quad (2.15)$$

Now the contributions of phase and amplitude variations are split up: the first term describes the energy cost of variations in the phase of the order parameter and the second term describes the energy cost of variations in the magnitude of the order parameter.

The dominating fluctuation is determined by the ratio of the factors $\frac{\hbar^2}{2m^*}$ and r , which has the dimension $(\text{Length})^2$, from which one can define the correlation length [33]

$$\xi = \sqrt{\frac{\hbar^2}{2m^*|r|}} = \xi_0 \left(1 - \frac{T}{T_C}\right)^{-\frac{1}{2}} \quad (2.16)$$

with the zero temperature value defined as the coherence length $\xi_0 = \xi(T=0) = \sqrt{\frac{\hbar^2}{2maT_C}}$. On length scales above ξ , the physics is entirely controlled by the phase degrees of freedom, i.e.:

$$\begin{aligned} f_{GL} &= \frac{\hbar^2}{2m^*}|\Psi|^2(\nabla\phi)^2 + \text{const.} \\ &= \frac{\hbar^2}{4m^*}n_S(\nabla\phi)^2 + \text{const.} \\ &= D_S(\nabla\phi)^2 + \text{const.} \end{aligned} \quad (2.17)$$

where $\frac{n_S}{2} = |\Psi|^2$ is the density of single electrons which form the Cooper pairs, also called the superfluid or superconducting density. Equation (2.17) shows that twisting the phase of the condensate is associated with an energy cost. This energy cost is characterized by the superfluid phase stiffness D_S .

Assuming frozen amplitude fluctuations $\Delta|\Psi(\mathbf{r})| = 0$, the stationary point of eq. (2.15) is

$$|\Psi| = |\Psi_0| \sqrt{1 - \xi^2|\nabla\phi(\mathbf{r})|^2}. \quad (2.18)$$

This shows that the superconducting order gets suppressed and eventually destroyed by short-ranged (below ξ) phase fluctuations. By introducing a particular form of phase fluctuations $\phi = \mathbf{q} \cdot \mathbf{r}$ into a microscopic model, it is possible to probe this breakdown of superconductivity and thus gain insight into the nature of superconductivity, in particular this gives access to ξ . This method will be explained further in a later section.

The discussion so far is valid for neutral superfluids, but superconductors are charged superfluids, so they couple to electromagnetic fields. The Ginzburg-Landau free energy with minimal coupling to an electromagnetic field is

$$f_{\text{GL}}[\Psi, \mathbf{A}] = \frac{\hbar^2}{2m^*} \left| \left(\nabla - \frac{ie^*}{\hbar} \mathbf{A} \right) \Psi \right|^2 + r|\Psi|^2 + \frac{u}{2}|\Psi|^4 + \frac{B^2}{2\mu_0}. \quad (2.19)$$

with an additional term to include the electromagnetic energy of the magnetic field $\mathbf{B} = \nabla \times \mathbf{A}$. It describes two intertwined Ginzburg-Landau theories for Ψ and \mathbf{A} . This means there are two length scales, the coherence length ξ governing amplitude fluctuations of Ψ and the London penetration depth λ_L which is associated with variations of the vector potential \mathbf{A} . This can be seen by considering a homogeneous condensate $\Psi = \sqrt{n_s/2}$, such that the free energy only depends on the vector potential as

$$f_{\text{GL}}[\mathbf{A}] \sim \frac{e^2 n_s}{2m^*} A^2 + \frac{(\nabla \times \mathbf{A})^2}{2\mu_0} = \frac{1}{2\mu_0} \left(\frac{1}{\lambda_L^2} A^2 + (\nabla \times \mathbf{A})^2 \right) \quad (2.20)$$

with the London penetration depth

$$\lambda_L = \sqrt{\frac{m^*}{e^2 n_s \mu_0}} \quad (2.21)$$

as the prefactor of A^2 , i.e. it is associated with the variations of \mathbf{A} . It is connected to the condensate stiffness as

$$\lambda_L = \sqrt{\frac{m^*}{e^2 n_s \mu_0}} = \sqrt{\frac{\hbar^2}{4e^2 \mu_0} \frac{4m^*}{\hbar^2 n_s}} = \sqrt{\frac{\hbar^2}{4e^2 \mu_0} \frac{1}{D_s}}, \quad (2.22)$$

see eq. (2.17).

The current density can be calculated from the stationary point condition of the free energy w.r.t. the vector potential \mathbf{A}

$$\frac{\delta f_{\text{GL}}}{\delta \mathbf{A}} = -\mathbf{j} + \frac{1}{\mu_0} \nabla \times \mathbf{B} \stackrel{!}{=} 0 \quad (2.23)$$

defining the supercurrent density

$$\mathbf{j} = -i \frac{e\hbar}{m^*} (\Psi^* \nabla \Psi - \Psi \Delta \Psi^*) - \frac{4e^2}{m^*} |\Psi|^2 \mathbf{A}. \quad (2.24)$$

Introducing the order parameter with a fixed phase $\Psi = |\Psi| e^{i\phi}$ gives

$$\mathbf{j} = 2e|\Psi|^2 \frac{\hbar}{m^*} \left(\nabla \phi - \frac{2\pi}{\Phi_0} \mathbf{A} \right) \quad (2.25)$$

with the magnetic flux quantum $\Phi_0 = \frac{\pi\hbar}{e}$. This shows that not only an applied field \mathbf{A} can induce a supercurrent, but also the phase twist $\nabla\phi$ of the condensate ground state, which is the remarkable property of superconductors enabling the dissipationless current. Where a conventional current is achieved by excitations above the ground state, the superflow is achieved through deformation of the ground-state phase. The supercurrent can be gauge-transformed to

$$\mathbf{j} = -\frac{4e^2 n_S}{m^*} \mathbf{A} = \tilde{D}_S \mathbf{A} \quad (2.26)$$

which shows that the superfluid phase stiffness

$$D_S = \frac{\hbar^2}{(2e)^2} \tilde{D}_S \quad (2.27)$$

also encodes the linear response of a system to a small applied vector field \mathbf{A} .

Calculating Superconducting Length Scales

As previously discussed in the context of eq. (2.18), analyzing the breakdown of the order parameter with phase fluctuations provides insight into the coherence length ξ_0 and the London penetration depth λ_L . A particular choice of phase fluctuations would be

$$\phi(\mathbf{r}) = \mathbf{q} \cdot \mathbf{r}, \quad (2.28)$$

which corresponds to Cooper pairs with a finite center-of-mass momentum \mathbf{q} . Although Cooper pairs typically do not carry such momentum in most materials, superconducting states with finite momentum can emerge under the influence of external fields or magnetism [42–44].

This approach for examining superconducting length scales that was developed by Witt et al. [18]. The authors used the method to characterize superconductivity in alkali-doped fullerides and find that via multiorbital effects, a superconducting state emerges that is characterized by a short coherence length yet robust stiffness, alongside a domeless increase in critical temperature with increasing pairing interaction. This is in contrast to the usual BCS-BEC crossover phenomenology that can be seen in unconventional superconductors, where with increasing pairing interaction there is a maximum of the critical temperature.

This section introduces the method within the framework of Ginzburg-Landau theory. The integration of this method into microscopic theories such as BCS theory and DMFT will be covered in the respective subsequent sections.

The phase fluctuation in eq. (2.28) corresponds to Fulde–Ferrell (FF) type pairing [45]

$$\Psi_{\mathbf{q}}(\mathbf{r}) = |\Psi_{\mathbf{q}}| e^{i\mathbf{qr}}. \quad (2.29)$$

With that, the free energy density eq. (2.13) is

$$f_{GL}[\Psi_{\mathbf{q}}] = r|\Psi_{\mathbf{q}}|^2 + \frac{u}{2}|\Psi_{\mathbf{q}}|^4 + \frac{\hbar^2 q^2}{2m^*}|\Psi_{\mathbf{q}}|^2. \quad (2.30)$$

The stationary point of the system can again be found via the condition

$$\frac{\delta f_{GL}}{\delta \Psi_{\mathbf{q}}^*} = 2\Psi_{\mathbf{q}} \left[r(1 - \xi^2 q^2) + u|\Psi_{\mathbf{q}}|^2 \right] = 0, \quad (2.31)$$

which results in the \mathbf{q} -dependence of the order parameter

$$|\Psi_{\mathbf{q}}|^2 = |\Psi_0|^2 (1 - \xi(T)^2 q^2). \quad (2.32)$$

This can be seen in fig. 2.2a. So for some value \mathbf{q}_c , the kinetic energy from phase modulations exceeds the gain in energy from pairing and superconducting order breaks down

$$\Psi_{\mathbf{q}_c} = 0. \quad (2.33)$$

So in Ginzburg-Landau theory the correlation length can be calculated via

$$q_c = \xi(T)^{-1}. \quad (2.34)$$

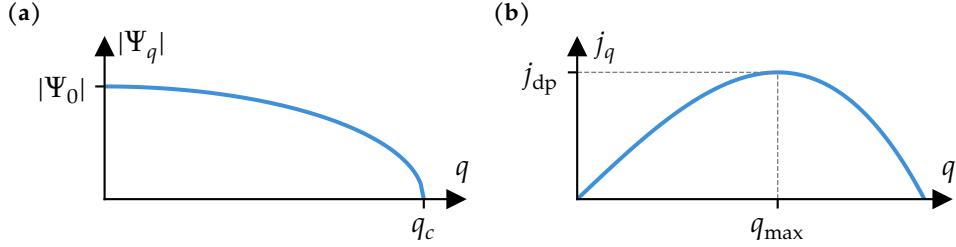


Figure 2.2 – Ginzburg-Landau solutions for a finite momentum q . (a) Breakdown of the order parameter with q , the critical q_c is the point at which the order parameter is 0. (b) Superconducting current coming from the finite momentum of the Cooper pairs. The maximum of the current with q is called the depairing current j_{dp} .

The temperature dependence of the $\xi(T)$ then gives access to the coherence length via eq. (2.16)

$$\xi(T) = \xi_0 \left(1 - \frac{T}{T_C}\right)^{-\frac{1}{2}} \quad (2.35)$$

Equation (2.24) shows that the momentum of the Cooper pairs entails a supercurrent \mathbf{j}_q . With $\phi(\mathbf{r}) = \mathbf{q} \cdot \mathbf{r}$ and $\mathbf{A} = 0$, the current is

$$\mathbf{j}_q = \frac{2\hbar e}{m^*} |\Psi_q|^2 \mathbf{q} . \quad (2.36)$$

The current \mathbf{j}_q is a non-monotonous function of \mathbf{q} with a maximum called the depairing current j_{dp} as can be seen in fig. 2.2b. The depairing current is an upper boundary for the maximal current that can flow through a material, also called the critical current j_c . The value of j_c is strongly dependent on the geometry of the sample [46, 47], so j_{dp} is not necessarily experimentally available, but it can be used to calculate the London penetration depth [34]

$$\lambda_L(T) = \sqrt{\frac{\Phi_0}{3\sqrt{3}\pi\mu_0\xi(T)j_{dp}(T)}} = \lambda_{L,0} \left(1 - \left(\frac{T}{T_C}\right)\right)^{-\frac{1}{2}} . \quad (2.37)$$

The superfluid phase stiffness can then be calculated via eq. (2.22)

$$D_S \propto \lambda_L^{-2} . \quad (2.38)$$

The finite-momentum method in the limit of $\mathbf{q} \rightarrow 0$ is related to linear response techniques to calculate the superfluid weight [26, 28].

2.2 Bardeen-Cooper-Schrieffer Theory

The BCS description of superconductivity was the first microscopic theory, identifying condensation of electrons into pairs forming a macroscopic quantum state as the underlying mechanism [10]. The BCS-Hamiltonian is

$$H_{\text{BCS}} = \sum_{\mathbf{k}\sigma} \epsilon_{\mathbf{k}\sigma} c_{\mathbf{k}\sigma}^\dagger c_{\mathbf{k}\sigma} + \sum_{\mathbf{k}, \mathbf{k}'} V_{\mathbf{k}, \mathbf{k}'} c_{\mathbf{k}\uparrow}^\dagger c_{-\mathbf{k}\downarrow}^\dagger c_{-\mathbf{k}'\downarrow} c_{\mathbf{k}'\uparrow}, \quad (2.39)$$

where $V_{\mathbf{k}, \mathbf{k}'}$ is a model interaction. It describes a phonon-mediated attractive interaction for energies lower than the Debye frequency ω_D :

$$V_{\mathbf{k}, \mathbf{k}'} = \begin{cases} -V_0 & (|\epsilon_{\mathbf{k}|}, |\epsilon_{\mathbf{k}'|} | < \omega_D) \\ 0 & (\text{otherwise}) \end{cases} \quad (2.40)$$

with $V_0 > 0$. The BCS Hamiltonian can be treated in a mean-field approach, writing

$$\begin{aligned} \sum_{\mathbf{k}, \mathbf{k}'} V_{\mathbf{k}, \mathbf{k}'} c_{\mathbf{k}\uparrow}^\dagger c_{-\mathbf{k}\downarrow}^\dagger c_{-\mathbf{k}'\downarrow} c_{\mathbf{k}'\uparrow} &\approx \sum_{\mathbf{k}, \mathbf{k}'} V_{\mathbf{k}, \mathbf{k}'} \langle c_{\mathbf{k}\uparrow}^\dagger c_{-\mathbf{k}\downarrow}^\dagger \rangle c_{-\mathbf{k}'\downarrow} c_{\mathbf{k}'\uparrow} + V_{\mathbf{k}, \mathbf{k}'} c_{\mathbf{k}\uparrow}^\dagger c_{-\mathbf{k}\downarrow}^\dagger \langle c_{-\mathbf{k}'\downarrow} c_{\mathbf{k}'\uparrow} \rangle \\ &= \sum_{\mathbf{k}} \Delta_{\mathbf{k}}^* c_{-\mathbf{k}\downarrow} c_{\mathbf{k}\uparrow} + \Delta_{\mathbf{k}} c_{\mathbf{k}\uparrow}^\dagger c_{-\mathbf{k}\downarrow}^\dagger \end{aligned} \quad (2.41)$$

with the pairing amplitude

$$\Delta_{\mathbf{k}} = \sum_{\mathbf{k}'} V_{\mathbf{k}, \mathbf{k}'} \langle c_{-\mathbf{k}'\downarrow} c_{\mathbf{k}'\uparrow} \rangle, \quad (2.42)$$

which is also the order parameter in BCS theory. A finite Δ corresponds to the pairing introduced above: it means there is a finite expectation value for a coherent creation/annihilation of electron pairs with opposite momentum and spin.

BCS theory was very successful in two ways: on the one hand it could quantitatively explain effects in the superconductors known at the time, for example the Hebel-Slichter peak that was measured in 1957 [48, 49] and the band gap measured by Giaever in 1960 [50]. On the other hand it gave a microscopic

explanation for the phenomenological theories of superconductivity based on F. Londons 1937 description of a quantum-mechanical wave function with a defined phase [9]. This picture of electron pairing still holds today even for superconductors that cannot be described by BCS theory [51].

There exist many textbooks tackling BCS theory from different angles, such as refs. [33, 34]. This section will use the ideas from BCS theory to treat superconductivity in the attractive Hubbard model on a mean-field level.

Multiband BCS Theory for the Attractive Hubbard Model

The Hubbard model is regarded as the simplest model for interacting electron systems. It goes back to works by Hubbard [52], Kanamori [53] and Gutzweiler [54] in the 1960s. The Hamiltonian of the single-band Hubbard model is

$$H = H_0 + H_{\text{int}} = \sum_{\langle ij \rangle \sigma} (-t_{ij} - \mu \delta_{ij}) c_{i\sigma}^\dagger c_{j\sigma} + \text{h.c.} + U \sum_i c_{i\uparrow}^\dagger c_{i\downarrow}^\dagger c_{i\downarrow} c_{i\uparrow} \quad (2.43)$$

where $U > 0$. The interaction describes a repulsive interaction between electrons of different spin at the same lattice site.

The Hubbard interaction is localized to one lattice site, so the Hubbard model emphasizes the electronic correlations. With the discovery of high T_C superconductors in the Cuprates, it was quickly realized that the 2D Hubbard model in the intermediate to strong-coupling regime has similar characteristics: parameter regimes with $d_{x^2-y^2}$ superconductivity, strong antiferromagnetic correlations, stripe order, pseudogaps, Fermi liquid and bad metallic behavior, with the phase diagram lines and observables being similar as a function of doping and temperature [55, 56]. Besides the relevancy for the Cuprates, having few parameters and simultaneously a very rich phase diagram with a variety of many-body effects also made the Hubbard model a perfect playground for new numerical tools, among them diagonalization, diagrammatics, Quantum Monte Carlo (QMC) methods and DMFT (see section 2.3).

The Hubbard model in the form of eq. (2.43) can be varied in a multitude of ways to model different physical systems, in this thesis to include multiple orbitals (i.e. atoms in the unit cell for lattice systems) and considering a purely attractive interaction. The local attractive interaction in this extended Hubbard model is useful as a model with a simple set of parameters to study superconductivity in systems where electrons experience a strong local attractive

interaction mediated through phonon degrees of freedom or with electronic excitations [57]. The form of the Hubbard Hamiltonian is then

$$H = \sum_{\langle i\alpha j\beta \rangle \sigma} (-t_{i\alpha, j\beta} - \mu_\sigma \delta_{i\alpha, j\beta}) c_{i\alpha\sigma}^\dagger c_{j\beta\sigma} + \text{h.c.} - \sum_{i,\alpha} U_\alpha c_{i\alpha\uparrow}^\dagger c_{i\alpha\downarrow}^\dagger c_{i\alpha\downarrow} c_{i\alpha\uparrow}, \quad (2.44)$$

where α counts orbitals and the minus sign in front of the interaction term is taken as a convention so that $U > 0$ now corresponds to an attractive interaction.

Mean field expression for Hubbard int

$$H_{\text{int}} \approx - \sum_{i,\alpha} U_\alpha (d_{i\alpha} \langle c_{i\alpha\downarrow} c_{i\alpha\uparrow} \rangle + e_{i\alpha} \langle c_{i\alpha\uparrow}^\dagger c_{i\alpha\downarrow}^\dagger \rangle + \langle c_{i\alpha\uparrow}^\dagger c_{i\alpha\downarrow}^\dagger \rangle \langle c_{i\alpha\downarrow} c_{i\alpha\uparrow} \rangle) \quad (2.45)$$

$$= - \sum_{i,\alpha} U_\alpha (c_{i\alpha\uparrow}^\dagger c_{i\alpha\downarrow}^\dagger \langle c_{i\alpha\downarrow} c_{i\alpha\uparrow} \rangle + c_{i\alpha\downarrow} c_{i\alpha\uparrow} \langle c_{i\alpha\uparrow}^\dagger c_{i\alpha\downarrow}^\dagger \rangle - \langle c_{i\alpha\uparrow}^\dagger c_{i\alpha\downarrow}^\dagger \rangle \langle c_{i\alpha\downarrow} c_{i\alpha\uparrow} \rangle) \quad (2.46)$$

$$= \sum_{i,\alpha} \left(\Delta_{i\alpha} c_{i\alpha\uparrow}^\dagger c_{i\alpha\downarrow}^\dagger + \Delta_{i\alpha}^* c_{i\alpha\downarrow} c_{i\alpha\uparrow} - \frac{|\Delta_{i\alpha}|^2}{U_\alpha} \right) \quad (2.47)$$

with the local superconducting order parameter

$$\Delta_{i,\alpha} = -U_\alpha \langle c_{i\alpha\downarrow} c_{i\alpha\uparrow} \rangle. \quad (2.48)$$

This results in the mean-field Hamiltonian

$$H_{\text{MF}} = \sum_{\langle i\alpha j\beta \rangle \sigma} (-t_{i\alpha, j\beta} - \mu_\sigma \delta_{i\alpha, j\beta}) c_{i\alpha,\sigma}^\dagger c_{j\beta,\sigma} + \text{h.c.} + \sum_{i,\alpha} \left(\Delta_{i\alpha} c_{i\alpha\uparrow}^\dagger c_{i\alpha\downarrow}^\dagger + \Delta_{i\alpha}^* c_{i\alpha\downarrow} c_{i\alpha\uparrow} - \frac{|\Delta_{i\alpha}|^2}{U_\alpha} \right) \quad (2.49)$$

The finite momentum is included as

$$\Delta_{i,\alpha} = \Delta_\alpha e^{i\mathbf{q}\mathbf{r}_{i\alpha}}. \quad (2.50)$$

The mean-field Hamiltonian can be written in momentum space using the Fourier transform

$$c_{i\alpha\sigma} = \frac{1}{\sqrt{N}} \sum_{\mathbf{k}} e^{i\mathbf{k}\mathbf{r}_{i\alpha}} c_{\mathbf{k}\alpha\sigma}, \quad (2.51)$$

with position vectors $\mathbf{r}_{i\alpha} = \mathbf{R}_i + \delta_\alpha$, written using the position of the unit cell \mathbf{R}_i and the orbital position inside the unit cell δ_α . Using this, the mean-field Hamiltonian is

$$H_{\text{MF}}(\mathbf{q}) = \sum_{\mathbf{k}} \Psi_{\mathbf{q},\mathbf{k}}^\dagger H_{\text{BdG}}(\mathbf{q},\mathbf{k}) \Psi_{\mathbf{q},\mathbf{k}} + K_{\mathbf{q}} \quad (2.52)$$

with the Nambu spinors

$$\Psi_{\mathbf{q},\mathbf{k}} = \begin{pmatrix} c_{\mathbf{k}1\uparrow} & c_{\mathbf{k}2\uparrow} & \dots & c_{\mathbf{k}n_{\text{orb}}\uparrow} & c_{\mathbf{q}-\mathbf{k}1\downarrow}^\dagger & c_{\mathbf{q}-\mathbf{k}2\downarrow}^\dagger & \dots & c_{\mathbf{q}-\mathbf{k}n_{\text{orb}}\downarrow}^\dagger \end{pmatrix}^T \quad (2.53)$$

and

$$K_{\mathbf{q}} = \sum_{\mathbf{k}} \text{Tr}[H_{\mathbf{k}}^\dagger] - n_{\text{orb}} N \mu - N \sum_{\alpha} \frac{|\Delta_\alpha(\mathbf{q})|^2}{U}. \quad (2.54)$$

The matrix between the spinors is the so-called Bogoliubov-de Gennes (BdG) matrix

$$H_{\text{BdG}}(\mathbf{q},\mathbf{k}) = \begin{pmatrix} H_{\mathbf{k}}^\dagger - \mu & \Delta(\mathbf{q}) \\ \Delta^\dagger(\mathbf{q}) & -\left(H_{\mathbf{q}-\mathbf{k}}^\dagger\right)^* + \mu \end{pmatrix} \quad (2.55)$$

with $H_{\mathbf{k}}$ being the Fourier transform of the kinetic term

$$[H_{\mathbf{k}}]_{\alpha\beta} = \sum_i t_{i\alpha,0\beta} e^{-i\mathbf{k}\cdot(\mathbf{R}_i+\delta_\alpha-\delta_\beta)} \quad (2.56)$$

and the matrix of order parameters, with the \mathbf{q} -dependence made explicit:

$$\Delta = \text{diag}(\Delta_1(\mathbf{q}), \Delta_2(\mathbf{q}), \dots, \Delta_{n_{\text{orb}}}(\mathbf{q})). \quad (2.57)$$

For time-reversal symmetric systems, there exists a solution such that all Δ_α are real [26] but the introduction of a finite \mathbf{q} breaks time-reversal symmetry. This means that in a multiband system, the order parameters in the orbital can develop different phases.

In the BdG formulation, the problem is now reduced to diagonalization of the matrix in eq. (2.55), so one can write

$$H_{\text{BdG}} = U_{\mathbf{q},\mathbf{k}} \epsilon_{\mathbf{q},\mathbf{k}} U_{\mathbf{q},\mathbf{k}}^\dagger \quad (2.58)$$

with the diagonal matrix $\epsilon_{\mathbf{q},\mathbf{k}} = \text{diag}(\epsilon_1(\mathbf{q},\mathbf{k}), \epsilon_2(\mathbf{q},\mathbf{k}), \dots, \epsilon_{2\cdot n_{\text{orb}}}(\mathbf{q},\mathbf{k}))$.

Equation (2.58) is a linear transformation from the creation and annihilation to a new set of operators

$$\gamma_{\mathbf{q},\mathbf{k}} = \begin{pmatrix} \gamma_{\mathbf{q},\mathbf{k},1} & \gamma_{\mathbf{q},\mathbf{k},2} & \dots & \gamma_{\mathbf{q},\mathbf{k},2 \cdot n_{\text{orb}}} \end{pmatrix}^T \quad (2.59)$$

via

$$\gamma_{\mathbf{q},\mathbf{k}} = U_{\mathbf{q},\mathbf{k}}^\dagger \Psi_{\mathbf{q},\mathbf{k}} \quad (2.60)$$

which define non-interacting quasi-particles. Using these operators, the mean-field Hamiltonian becomes

$$H_{\text{MF}}(\mathbf{q}) = \sum_{\mathbf{k}} \gamma_{\mathbf{q},\mathbf{k}} \epsilon_{\mathbf{q},\mathbf{k}} \gamma_{\mathbf{q},\mathbf{k}}^\dagger \quad (2.61)$$

Mean-field theory does not give a value for the order parameter a priori, it needs to be calculated self-consistently using the gap equation

$$\begin{aligned} \Delta_\alpha &= -U_\alpha \langle c_{i\alpha\downarrow} c_{i\alpha\uparrow} \rangle = -\frac{U}{N} \sum_{\mathbf{k}} \langle c_{\mathbf{k}\alpha\downarrow} c_{-\mathbf{k}\alpha\uparrow} \rangle \\ &= -\frac{U}{N} \sum_{\mathbf{k}} \sum_{ij} [U_{\mathbf{q},\mathbf{k}}]_{i,\alpha+n_{\text{orb}}} [U_{\mathbf{q},\mathbf{k}}^\dagger]_{\alpha,j} \langle \gamma_i^\dagger \gamma_j \rangle \\ &= -\frac{U}{N} \sum_{\mathbf{k}} [U_{\mathbf{q},\mathbf{k}} n_F(\epsilon_{\mathbf{q},\mathbf{k}}) U_{\mathbf{q},\mathbf{k}}^\dagger]_{\alpha,\alpha+n_{\text{orb}}} . \end{aligned} \quad (2.62)$$

This means starting from an initial value, the BdG matrix needs to be set up, diagonalized and then used to determine Δ_α again, until a converged value is found.

To implement the finite \mathbf{q} method to calculate the superconducting length scales, one also needs access to the supercurrent in BCS theory. This approach for calculating the current is generalized for the multi orbital case from ref. [18].

In general, a current \mathbf{j} is induced by change of the local polarization \mathbf{P} . The polarization operator is

$$\hat{\mathbf{P}} = e \sum_{i\alpha} \mathbf{R}_{i\alpha} c_{i\alpha}^\dagger c_{i\alpha} = e \sum_{i\alpha} \mathbf{R}_{i\alpha} n_{i\alpha} , \quad (2.63)$$

so that the current given by the time derivative of the polarization operator is

$$\hat{\mathbf{j}} = \dot{\hat{\mathbf{P}}} = \frac{i}{\hbar} [\hat{\mathbf{P}}, H] . \quad (2.64)$$

Taking a Hamiltonian with pairing $\Delta_{i\alpha}$

$$H = \sum_{(i\alpha j\beta)\sigma} -t_{i\alpha, j\beta} c_{i\alpha\sigma}^\dagger c_{j\beta\sigma} + \sum_{i,\alpha} (\Delta_{i\alpha} c_{i\alpha\uparrow}^\dagger c_{i\alpha\downarrow}^\dagger + \Delta_{i\alpha}^* c_{i\alpha\downarrow} c_{i\alpha\uparrow}) =: H_N + H_{AN} \quad (2.65)$$

one needs to calculate three kinds of commutators for eq. (2.64):

$$[n_{m\gamma}, c_{i\alpha}^\dagger c_{j\beta}] = c_{i\alpha}^\dagger [n_{m\gamma}, c_{j\beta}] + [n_{m\gamma}, c_{i\alpha}^\dagger] c_{j\beta} = (\delta_{m\gamma, i\alpha} - \delta_{m\gamma, j\beta}) c_{i\alpha}^\dagger c_{j\beta} \quad (2.66)$$

$$[n_{m\gamma}, c_{i\alpha} c_{i\alpha}] = c_{i\alpha} [n_{m\gamma}, c_{i\alpha}] + [n_{m\gamma}, c_{i\alpha}] c_{i\alpha} = -2\delta_{m\gamma, i\alpha} c_{i\alpha} c_{i\alpha} \quad (2.67)$$

$$[n_{m\gamma}, c_{i\alpha}^\dagger c_{i\alpha}^\dagger] = c_{i\alpha}^\dagger [n_{m\gamma}, c_{i\alpha}^\dagger] + [n_{m\gamma}, c_{i\alpha}^\dagger] c_{i\alpha}^\dagger = 2\delta_{m\gamma, i\alpha} c_{i\alpha}^\dagger c_{i\alpha}^\dagger. \quad (2.68)$$

Using these, the normal and anomalous component of the current can be calculated:

$$\begin{aligned} \hat{\mathbf{j}}_N &= \frac{i}{\hbar} [\hat{\mathbf{P}}, H_N] = -i\frac{e}{\hbar} \sum_{i\alpha, j\beta, m\gamma} \mathbf{R}_{m\gamma} t_{i\alpha, j\beta} [n_{m\gamma}, c_{i\alpha}^\dagger c_{j\beta}] \\ &= -i\frac{e}{\hbar} \sum_{i\alpha, j\beta, m\gamma} \mathbf{R}_{m\gamma} t_{i\alpha, j\beta} (\delta_{m\gamma, i\alpha} - \delta_{m\gamma, j\beta}) c_{i\alpha}^\dagger c_{j\beta} \\ &= -i\frac{e}{\hbar} \sum_{i\alpha, j\beta} (\mathbf{R}_{i\alpha} - \mathbf{R}_{j\beta}) t_{i\alpha, j\beta} c_{i\alpha}^\dagger c_{j\beta} \end{aligned} \quad (2.69)$$

and

$$\begin{aligned} \hat{\mathbf{j}}_{AN} &= \frac{i}{\hbar} [\hat{\mathbf{P}}, H_{AN}] = -i\frac{e}{\hbar} \sum_{i\alpha, m\gamma} \mathbf{R}_{m\gamma} (\Delta_{i\alpha} [n_{m\gamma}, c_{i\alpha} c_{i\alpha}] + \Delta_{i\alpha}^* [n_{m\gamma}, c_{i\alpha}^\dagger c_{i\alpha}^\dagger]) \\ &= -i\frac{2e}{\hbar} \sum_{i\alpha, m\gamma} \mathbf{R}_{m\gamma} (-\delta_{m\gamma, i\alpha} \Delta_{i\alpha} c_{i\alpha} c_{i\alpha} + \delta_{m\gamma, i\alpha} \Delta_{i\alpha}^* c_{i\alpha}^\dagger c_{i\alpha}^\dagger) \\ &= i\frac{2e}{\hbar} \sum_{i\alpha} \mathbf{R}_{i\alpha} (-\Delta_{i\alpha} c_{i\alpha} c_{i\alpha} + \Delta_{i\alpha}^* c_{i\alpha}^\dagger c_{i\alpha}^\dagger). \end{aligned} \quad (2.70)$$

The expectation value of the anomalous part vanishes

$$\langle \hat{\mathbf{j}}_{AN} \rangle = i\frac{2e}{\hbar} \sum_{i\alpha} \mathbf{R}_{i\alpha} (-\Delta_{i\alpha} \langle c_{i\alpha} c_{i\alpha} \rangle + \Delta_{i\alpha}^* \langle c_{i\alpha}^\dagger c_{i\alpha}^\dagger \rangle) \quad (2.71)$$

$$= i\frac{2e}{\hbar} \sum_{i\alpha} \frac{\mathbf{R}_{i\alpha}}{U_\alpha} (\Delta_{i\alpha} \Delta_{i\alpha}^* - \Delta_{i\alpha}^* \Delta_{i\alpha}) = 0, \quad (2.72)$$

so that the current density is given by the normal component. Using the Fourier transform

$$c_{i\alpha\sigma} = \frac{1}{\sqrt{N}} \sum_{\mathbf{k}} e^{i\mathbf{k}\mathbf{r}_{i\alpha}} c_{\mathbf{k}\alpha\sigma}, \quad (2.73)$$

the current can be written as

$$\hat{\mathbf{j}} = \hat{\mathbf{j}}_N = i \frac{e}{\hbar N_k} \sum_{i\alpha, j\beta, \mathbf{k}\mathbf{k}'} (\mathbf{R}_{i\alpha} - \mathbf{R}_{j\beta}) t_{i\alpha, j\beta} e^{i(\mathbf{k}\mathbf{r}_{i\alpha} - \mathbf{k}'\mathbf{r}_{j\beta})} c_{\mathbf{k}\alpha}^\dagger c_{\mathbf{k}'\beta} \quad (2.74)$$

$$= i \frac{e}{\hbar N_k} \sum_{i\alpha, j\beta, \mathbf{k}\mathbf{k}'} (\mathbf{R}_{i\alpha} - \mathbf{R}_{j\beta}) t_{i\alpha, j\beta} e^{i(\mathbf{k}\mathbf{r}_{i\alpha} - \mathbf{k}'\mathbf{r}_{j\alpha})} c_{\mathbf{k}\alpha}^\dagger c_{\mathbf{k}'\beta} \quad (2.75)$$

$$\stackrel{\mathbf{r}_{i\alpha} \mapsto \mathbf{r}_{i\alpha} + \mathbf{r}_{j\beta}}{=} i \frac{e}{\hbar N_k} \sum_{\mathbf{r}_{i\alpha} \mathbf{k}\mathbf{k}' \alpha \beta \sigma} \mathbf{R}_{i\alpha} t_{i\alpha, j\beta} \sum_{\mathbf{r}_{j\beta}} e^{i(\mathbf{k} - \mathbf{k}')\mathbf{r}_{j\beta}} c_{\mathbf{k}\alpha}^\dagger c_{\mathbf{k}'\beta} \quad (2.76)$$

$$= \frac{e}{\hbar N_k} \sum_{\mathbf{k}\alpha\beta\sigma} i \sum_{\mathbf{r}_{i\alpha}} \mathbf{r}_{i\alpha} t_{i\alpha\beta} e^{i\mathbf{k}\mathbf{r}_{i\alpha}} c_{\mathbf{k}\alpha}^\dagger c_{\mathbf{k}\beta} = \frac{e}{\hbar N_k} \sum_{\mathbf{k}\alpha\beta\sigma} \nabla_{\mathbf{k}} h(\mathbf{k})_{\alpha\beta} c_{\mathbf{k}\alpha}^\dagger c_{\mathbf{k}\beta} \quad (2.77)$$

$$:= \frac{e}{N_k} \sum_{\mathbf{k}\alpha\beta\sigma} \mathbf{v}_{\alpha\beta} c_{\mathbf{k}\alpha}^\dagger c_{\mathbf{k}\beta} \quad (2.78)$$

This means current density is

$$\mathbf{j}_{\mathbf{q}} = \langle \hat{\mathbf{j}} \rangle_{\mathbf{q}} = \frac{e}{N_k} \sum_{\mathbf{k}\alpha\beta\sigma} \mathbf{v}_{\alpha\beta}(\mathbf{k}) \langle c_{\mathbf{k}\alpha\sigma}^\dagger c_{\mathbf{k}\beta\sigma} \rangle_{\mathbf{q}} = \frac{2e}{N_k} \sum_{\mathbf{k}\alpha\beta} \mathbf{v}_{\alpha\beta}(\mathbf{k}) \langle c_{\mathbf{k}\alpha\uparrow}^\dagger c_{\mathbf{k}\beta\downarrow} \rangle_{\mathbf{q}}, \quad (2.79)$$

which can be expressed using the BdG energies

$$\mathbf{j}_{\mathbf{q}} = \frac{2e}{N_k} \sum_{\mathbf{k}\alpha\beta n} \mathbf{v}_{\alpha\beta}(\mathbf{k}) [U_{\mathbf{q}\mathbf{k}}]_{\alpha n} [U_{\mathbf{q}\mathbf{k}}^*]_{\beta n} n_F(E_n), \quad (2.80)$$

where $n \in \{1, \dots, 2N_{\text{orb}}\}$.

2.3 Dynamical Mean-Field Theory

The foundational idea of DMFT is to map the full interacting problem to the problem of a single lattice site (or a small cluster of lattice sites) embedded in a mean field encompassing all non-local correlation effects. This mapping can be seen in fig. 2.3. In contrast to static mean-field theories such as BCS theory,

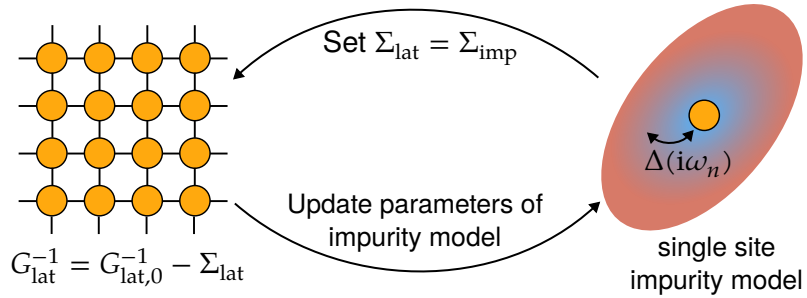


Figure 2.3 – Mapping of the full lattice problem onto a single-site impurity model. This also visualizes the DMFT self-consistency loop: Coming from the full lattice problem, an impurity model is set up, which is then solved to get the self-energy Σ_{imp} , which encompasses all interaction effects. The loop is converged when $\Sigma_{\text{lat}} = \Sigma_{\text{imp}}$, otherwise the impurity self-energy is a new guess for the self-energy of the lattice problem.

DMFT treats all local correlations. When the interaction strength becomes comparable to the kinetic energy of the electrons, the electrons are becoming increasingly localized and the band structure picture is not applicable anymore. One hallmark effect in this strongly-correlated regime is the interaction driven metal-insulator (Mott) transition. Using DMFT, the Mott transition seen in materials like V_2O_3 [58] can be explained in the Hubbard model [59].

In this section I will describe the Green's function formalism, the mapping of the lattice problem onto the impurity problem and the resulting self-consistency loop of DMFT. Additionally, I will also describe how to treat the superconducting state in terms of Green's function and the consequences for the DMFT self-consistency condition. I will not fully derive the equations of DMFT here, for a more expansive introduction see refs. [33, 35, 60, 61].

Green's Function Formalism

Green's functions are a method to encode influence of many-body effects on propagation of particles in a system. Depending on the context different kinds of Green's functions are employed. Matsubara Green's functions naturally includes finite temperatures, which is done via a Wick rotation of the time

variable t into imaginary time

$$t \rightarrow -i\tau \quad (2.81)$$

where τ is real and has the dimension time. This enables the simultaneous expansion of exponential $e^{-\beta H}$ coming from the thermodynamic average and e^{-iHt} coming from the time evolution of operators. Matsubara Greens function are defined as

$$G_{\alpha_1\alpha_2}(\tau_1, \tau_2) = -\langle T_\tau(c_{\alpha_1}(\tau_1)c_{\alpha_2}^\dagger(\tau_2)) \rangle \quad (2.82)$$

with:

- $c_\alpha, c_\alpha^\dagger$ fermionic creation/annihilation operators of quantum states α in the Heisenberg time-evolution picture $\hat{A}(\tau) = e^{\tau H} \hat{A} e^{-\tau H}$
- $\langle \cdot \rangle = \text{Tr}(\hat{\rho} \cdot)$ the thermal expectation value with statistical operator $\hat{\rho} = e^{-\beta H}/Z$ with partition function Z and Hamiltonian H
- Time-ordering operator

$$\begin{aligned} T_\tau(A(\tau)B(\tau')) &= \Theta(\tau - \tau')A(\tau)B(\tau') \pm \Theta(\tau' - \tau)B(\tau')A(\tau) \\ &= \begin{cases} A(\tau)B(\tau') & \text{if } \tau < \tau' \\ B(\tau')A(\tau) & \text{if } \tau' < \tau \end{cases} \end{aligned} \quad (2.83)$$

In thermal equilibrium, the Green's function only depends on time differences $\tau_1 - \tau_2$, so by defining $\tau = \tau_1 - \tau_2$, one can work with a single time.

Fermionic Matsubara Green's functions are antiperiodic in time with periodicity β . For $-\beta < 0 < 0$, the cyclic properties of the trace means that

$$G(\tau) = -G(\tau + \beta). \quad (2.84)$$

This means that the Green's functions can be restricted to the interval $0 < \tau < \beta$ and in turn, there is a Fourier expansion with discrete frequencies $\omega_n = (2n+1)\pi/\beta$:

$$G(i\omega_n) = \int_0^\beta d\tau G(\tau) e^{i\omega_n \tau} \quad (2.85)$$

$$G(\tau) = \frac{1}{\beta} \sum_n G(i\omega_n) e^{-i\omega_n \tau}. \quad (2.86)$$

In lattice system there is a spatial dependence $\alpha = \mathbf{R}$ and due to translational invariance, G only depends on $\mathbf{R}_1 - \mathbf{R}_2$. This means one can transform between real-space and crystal momentum representation as

$$G(\mathbf{k}) = \sum_i G(\mathbf{R}_i) e^{i\mathbf{k}\mathbf{R}_i} \quad (2.87)$$

$$G(\mathbf{r}) = \frac{1}{N_{\mathbf{k}}} \sum_{\mathbf{k}} G(\mathbf{k}) e^{-i\mathbf{k}\mathbf{r}}, \quad (2.88)$$

both in τ and Matsubara frequency space.

Matsubara Green's function make calculations computationally easier, but do not give information on experimental observables. This can be done by extending the description to real frequencies ω by analytic continuation [35]

$$G^R(\omega + i\eta) = G(i\omega_n \rightarrow \omega + i\eta), \quad (2.89)$$

where the $\eta > 0$ is an infinitesimal part. On real frequencies, the retarded Green's function G^R connects to experimentally measurable quantities, such as the spectral function

$$A(\omega, \mathbf{k}) = -\frac{1}{\pi} \Im(G(\omega + i\eta, \mathbf{k})), \quad (2.90)$$

describing the excitation spectrum of the system being measured.

Dyson Equation

A non-interacting system with dispersion $\epsilon_{\mathbf{k}}$ can be described by the free Green's function

$$G_0(i\omega_n, \mathbf{k}) = [i\omega_n - \epsilon_{\mathbf{k}}]^{(-1)} \quad (2.91)$$

The feedback of the environment on propagation of the particle is encoded in an object called the self-energy $\Sigma(i\omega_n, \mathbf{k})$. The interacting and non-interacting Green's function are connected by the Dyson equation

$$G = G_0 + G_0 \Sigma G. \quad (2.92)$$

The solution to the Dyson equation can formally be written as

$$G(i\omega_n, \mathbf{k}) = [G_0(i\omega_n, \mathbf{k}) - \Sigma(\mathbf{k}, i\omega_n)]^{-1}. \quad (2.93)$$

The real part of $\Sigma(\mathbf{k}, i\omega_n)$ describes renormalization of energy levels and the imaginary part describes the finite lifetime of quasiparticles.

The self-energy enables a systematic inclusion of interaction effects and approximations given certain system restraints. In DMFT, the self-energy is taken to be purely local, which is exact in the limit of infinite dimension, but it can still capture effects which depend significantly on local dynamic correlations in low-dimensional system.

Mapping to Impurity Model and DMFT Self-Consistency Loop

The central idea of DMFT is to map the full lattice problem onto a problem of a single impurity of the form

$$H_{\text{IM}} = H_{\text{imp}} + H_{\text{bath}} + H_{\text{hyb}} \quad (2.94)$$

with the terms

$$H_{\text{imp}} = \sum_{\alpha\sigma} \epsilon_{d,\alpha} d_{\alpha\sigma}^\dagger d_{\alpha\sigma} + \sum_{\alpha} U_{\alpha} n_{d,\alpha\uparrow} n_{d,\alpha\downarrow} \quad (2.95)$$

$$H_{\text{bath}} = \sum_{\mathbf{k},n\sigma} \epsilon_{\mathbf{k},n} c_{\mathbf{k}n\sigma}^\dagger c_{\mathbf{k}n\sigma} \quad (2.96)$$

$$H_{\text{hyb}} = \sum_{\mathbf{k},\alpha n\sigma} V_{\mathbf{k},\alpha n} d_{\alpha\sigma}^\dagger c_{\mathbf{k}n\sigma} + V_{\mathbf{k},n\alpha}^* c_{\mathbf{k}n\sigma}^\dagger d_{\alpha\sigma} \quad (2.97)$$

Here, d are the operators for the impurity site and c are the operators for the bath, which is characterized by the energy levels $\epsilon_{\mathbf{k},n}$ and hybridization to the impurity orbitals $V_{\mathbf{k},\alpha n}$.

Using the path-integral formalism, the bath degrees of freedom can be integrated out [61]:

$$S_{\text{imp}} = - \int_0^\beta d\tau d\tau' \sum_{\alpha\beta,\sigma} d_{\alpha\sigma}^*(\tau) [G_{\text{imp},0}^{-1}]_{\alpha\beta}(\tau - \tau') d_{\beta\sigma}(\tau') \quad (2.98)$$

$$+ \int_0^\beta d\tau \sum_{\alpha} U_{\alpha} n_{d,\alpha\uparrow} n_{d,\alpha\downarrow} \quad (2.99)$$

with the non-interacting impurity Green's function $G_{\text{imp},0}$, given by

$$[G_{\text{imp},0}]_{\alpha,\beta} = \left[i\omega_n - \epsilon_{d,\alpha} - \sum_{\mathbf{k}} \frac{V_{\mathbf{k},\alpha n}^* V_{\mathbf{k},n\beta}}{i\omega_n - \epsilon_{\mathbf{k},n}} \right] \quad (2.100)$$

The approximation of DMFT lies in the fact that the self-energy of the impurity model $\Sigma_{\text{imp}}(i\omega_n)$ is purely local, where the lattice self-energy $\Sigma_{\text{lat}}(i\omega_n, \mathbf{k})$ carries a \mathbf{k} -dependence. As shown in the illustration fig. 2.3, these two quantities are set equal to go from the impurity to the lattice model:

$$\Sigma_{\text{lat}}(i\omega_n, \mathbf{k}) \approx \Sigma_{\text{imp}}(i\omega_n) =: \Sigma(i\omega_n). \quad (2.101)$$

Using this, the local lattice Greens function is obtained by summing over the \mathbf{k} -dependence:

$$G_{\text{loc}}(i\omega_n) = \frac{1}{N_k} \sum_{\mathbf{k}} [i\omega_n - h(\mathbf{k}) - \Sigma(i\omega_n)]^{-1} \stackrel{!}{=} G_{\text{imp}}(i\omega_n). \quad (2.102)$$

By demanding that this is equal to the impurity Green's function G_{imp} , the mapping to the impurity model is defined. Using the Dyson equation, the non-interacting Greens function for the impurity problem can be calculated as

$$G_{\text{imp},0}(i\omega_n) = [G_{\text{loc}}^{-1}(i\omega_n) + \Sigma(i\omega_n)]^{-1}. \quad (2.103)$$

This sets up an impurity model which can be solved by computational means.

Given a solution to the impurity problem with has been found, this interacting Green's function $G_{\text{imp}}(i\omega_n)$ can be used to calculate the self-energy via

$$\Sigma(i\omega_n) = G_{\text{imp},0}^{-1}(i\omega_n) - G_{\text{imp}}^{-1}(i\omega_n). \quad (2.104)$$

The DMFT self-consistency loop as shown in fig. 2.3 consists of the following steps:

1. Choose an initial self-energy Σ , for example $\Sigma = 0$.
2. Use eq. (2.102) to calculate $G_{\text{loc}}(i\omega_n)$.
3. Calculate the non-interacting impurity Green's function from eq. (2.103).
4. Solve the interacting impurity model, obtaining $G_{\text{imp}}(i\omega_n)$.
5. Calculate a new self-energy $\Sigma(i\omega_n)$ via eq. (2.104).
6. Check convergence of the self-energy (or alternatively via the condition $G_{\text{loc}}(i\omega_n) = G_{\text{imp}}(i\omega_n)$). Otherwise, use this self-energy as a new input in step 2.

Step 4, solving the impurity model is the computationally hardest step in the DMFT loop and many different solver methods have been developed over the years with differing use cases, accuracy and numerical demands.

The TRIQS toolkit [62] implements methods to work with Green's functions, using different impurity solvers to enable efficient development of DMFT methods. For the calculations in this thesis, Exact Diagonalization (ED) as implemented in the EDIpack library [63] has been used. It was made available to TRIQS via a compatibility layer by I. Krivenko and L. Crippa [64].

The idea of ED as introduced by Caffarel and Krauth [65] is to represent the bath with a finite number of discrete bath sites N_b . This means the Hamiltonian for the impurity model is adjusted to

$$H_{\text{bath}} = \sum_{\substack{k \in \{1, \dots, N_b\} \\ n\sigma}} \epsilon_{k,n} c_{kn\sigma}^\dagger c_{kn\sigma} \quad (2.105)$$

$$H_{\text{hyb}} = \sum_{\substack{k \in \{1, \dots, N_b\} \\ \alpha n\sigma}} V_{k,\alpha n} d_{\alpha\sigma}^\dagger c_{kn\sigma} + V_{k,n\alpha} c_{kn\sigma}^\dagger d_{\alpha\sigma} \quad (2.106)$$

In ED, one needs to fit the bath parameters $\{\epsilon_k, V_k\}$ to optimally represent the lattice system, i.e. find the best fit to approximate the hybridization function $\Delta(i\omega_n)$ of the impurity model by the discrete hybridization function

$$\Delta_{\{\epsilon_k, V_k\}}(i\omega_n) = \sum_{k=1}^{N_b} \frac{|V_k|^2}{i\omega_n - \epsilon_k} \quad (2.107)$$

containing only a finite amount of poles. This is implemented in EDIpack.

Nambu-Gorkov Green's Functions

To describe superconductivity in the Green's function formalism, one introduces the Nambu-Gor'kov formalism [61]. Using the Nambu spinors as in eq. (2.53)

$$\Psi_{\mathbf{k},\mathbf{q},\alpha} = \begin{pmatrix} c_{\mathbf{k}\alpha\uparrow} & c_{\mathbf{q}-\mathbf{k}\alpha\downarrow}^\dagger \end{pmatrix}^T, \quad (2.108)$$

the Green's functions become 2×2 matrices in Nambu space

$$[\mathcal{G}_{\mathbf{q}}(\tau, \mathbf{k})]_{\alpha\gamma} = -\langle T_{\tau} \Psi_{\mathbf{k}, \mathbf{q}, \alpha} \Psi_{\mathbf{k}, \mathbf{q}, \gamma}^{\dagger} \rangle \quad (2.109)$$

$$= \begin{pmatrix} -\langle T_{\tau} c_{\mathbf{k}, \alpha, \uparrow} c_{\mathbf{k}, \gamma, \uparrow}^{\dagger} \rangle & -\langle T_{\tau} c_{\mathbf{k}, \alpha, \uparrow} c_{\mathbf{q}-\mathbf{k}, \gamma, \downarrow} \rangle \\ -\langle T_{\tau} c_{\mathbf{q}-\mathbf{k}, \alpha, \downarrow}^{\dagger} c_{\mathbf{k}, \gamma, \uparrow} \rangle & -\langle T_{\tau} c_{\mathbf{q}-\mathbf{k}, \alpha, \downarrow} c_{\mathbf{q}-\mathbf{k}, \gamma, \downarrow}^{\dagger} \rangle \end{pmatrix} \quad (2.110)$$

$$= \begin{pmatrix} [\mathcal{G}_{\mathbf{q}}^{11}(\tau, \mathbf{k})]_{\alpha\gamma} & [\mathcal{G}_{\mathbf{q}}^{12}(\tau, \mathbf{k})]_{\alpha\gamma} \\ [\mathcal{G}_{\mathbf{q}}^{21}(\tau, \mathbf{k})]_{\alpha\gamma} & [\mathcal{G}_{\mathbf{q}}^{22}(\tau, \mathbf{k})]_{\alpha\gamma} \end{pmatrix}. \quad (2.111)$$

Due to the definition of the Nambu spinors with \mathbf{q} only appearing in the spin-down sector, only \mathcal{G}^{11} carries the \mathbf{q} -dependence. The superconducting state is marked by the fact that the so-called anomalous Green's functions $\mathcal{G}^{11}, \mathcal{G}^{12}$ are non-zero. On Matsubara frequencies, the Nambu-Gor'kov Green's functions is set up via

$$\begin{aligned} & [\mathcal{G}_{\mathbf{q}}(i\omega_n, \mathbf{k})]^{-1} \quad (2.112) \\ &= \begin{pmatrix} (i\omega_n + \mu) - h(\mathbf{k}) - \Sigma^N(i\omega_n) & -\Sigma^{AN}(i\omega_n) \\ -\Sigma^{AN}(i\omega_n) & (i\omega_n - \mu) + h(-\mathbf{k} + \mathbf{q}) + (\Sigma^N)^*(i\omega_n) \end{pmatrix} \end{aligned}$$

with the self-energy now being composed of a normal and anomalous part:

$$\mathcal{S}(i\omega_n) = \begin{pmatrix} \Sigma^N(i\omega_n) & \Sigma^{AN}(i\omega_n) \\ \Sigma^{AN}(i\omega_n) & -(\Sigma^N)^*(i\omega_n) \end{pmatrix} \quad (2.113)$$

The self-consistency cycle of DMFT introduced in the section above can equivalently be defined in Nambu space, replacing eqs. (2.102) to (2.104):

$$\begin{cases} \mathcal{G}_{loc}(i\omega_n) = \frac{1}{N_k} \sum_{\mathbf{k}} \mathcal{G}(i\omega_n, \mathbf{k}) \\ \mathcal{G}_{imp,0} = [\mathcal{G}_{loc}^{-1}(i\omega_n) + \mathcal{S}(i\omega_n)]^{-1} \\ \mathcal{S}(i\omega_n) = \mathcal{G}_{imp,0}^{-1}(i\omega_n) - \mathcal{G}_{imp}^{-1}(i\omega_n) \end{cases} \quad (2.114)$$

2.4 Quantum Geometry

An emerging topic in condensed matter physics is the fact that the geometric properties of the free electron ground state have influence on many (quantum) material properties [38, 66]. The first example of this was the 1980 discovery

of the Integer quantum Hall effect [67]. This was explained by Thouless et al. as being a consequence of the unique topology of the electronic ground state which is encoded by the Chern number \mathcal{C} [68]. The Chern number is an integer that is the result of the integration of the Berry curvature over the Brillouin zone. The Berry curvature describes the change of the eigenstate's phase as the momentum \mathbf{k} is varied and it is part of the quantum geometry of a material, the geometric structure in the space of quantum states when these states depend on a continuous parameter (lattice momentum \mathbf{k} for solids).

The concept of quantum geometry was first formulated in 1980 by Provost and Vallee [69]. The starting point is a parameter dependent Hamiltonian $\{H(\lambda)\}$ with a smooth dependence on a parameter $\lambda = (\lambda_1, \lambda_2, \dots) \in \mathcal{M}$ (\mathcal{M} is called the base manifold). The Hamiltonian acts on a parametrized Hilbert space $\mathcal{H}(\lambda)$ with eigenenergies $E_n(\lambda)$ and eigenstates $|\phi_n(\lambda)\rangle$. A system state $|\psi(\lambda)\rangle$ is a linear combination of $|\phi_n(\lambda)\rangle$ at every point in \mathcal{M} . On infinitesimal variation of the parameter $d\lambda$, the distance in the space of quantum states is

$$ds^2 = \|\psi(\lambda + d\lambda) - \psi(\lambda)\|^2 = \langle \delta\psi | \delta\psi \rangle \quad (2.115)$$

$$= \langle \partial_\mu \psi | \partial_\nu \psi \rangle d\lambda^\mu d\lambda^\nu = (\gamma_{\mu\nu} + i\sigma_{\mu\nu}) d\lambda^\mu d\lambda^\nu. \quad (2.116)$$

The imaginary part $\sigma_{\mu\nu}$ is the Berry curvature mentioned above. The real part $\gamma_{\mu\nu}$ is not gauge invariant, so in order to have a meaningful notion of a metric one needs to define the gauge invariant quantity

$$g_{\mu\nu} := \gamma_{\mu\nu} - \beta_\mu \beta_\nu. \quad (2.117)$$

where $\beta_\mu = i \langle \partial_\mu \psi | \psi \rangle$ is the Berry connection, which is purely real. For simplicity, one defines the quantum geometric tensor:

$$\mathcal{Q}_{\mu\nu}(\lambda) := \langle \partial_\mu \psi(\lambda) | \partial_\nu \psi(\lambda) \rangle - \langle \partial_\mu \psi(\lambda) | \psi(\lambda) \rangle \langle \psi(\lambda) | \partial_\nu \psi(\lambda) \rangle \quad (2.118)$$

where now

$$g_{\mu\nu} = \Re \mathcal{Q}_{\mu\nu}, \quad \sigma_{\mu\nu} = \Im \mathcal{Q}_{\mu\nu}. \quad (2.119)$$

In numerical calculations, the phases of neighboring states are random, so the derivatives of states in the quantum geometric tensor does not give definitive results. Instead, when the system is adiabatic, i.e. the system is restricted to a subspace $\mathcal{H}_{E_0}(\lambda)$ for an instantaneous eigenvalue of Hamiltonian

$$H(\lambda) |\phi_0(\lambda)\rangle = E_0(\lambda) |\phi_0(\lambda)\rangle, \quad (2.120)$$

one can connect to derivatives of the Hamiltonian. Without loss of generality, one can consider the ground state $|\phi_0(\lambda)\rangle$, for which the quantum geometric tensor is

$$\mathcal{Q}_{\mu\nu}(\lambda) = \langle \partial_\mu \phi_0(\lambda) | \partial_\nu \phi_0(\lambda) \rangle - \langle \partial_\mu \phi_0(\lambda) | \phi_0(\lambda) \rangle \langle \phi_0(\lambda) | \partial_\nu \phi_0(\lambda) \rangle \quad (2.121)$$

$$= \langle \partial_\mu \phi_0 | (1 - |\phi_0\rangle \langle \phi_0|) | \partial_\nu \phi_0 \rangle \quad (2.122)$$

$$= \sum_{n \neq 0} \langle \partial_\mu \phi_0 | \phi_n \rangle \langle \phi_n | \partial_\mu \phi_0 \rangle \quad (2.123)$$

The first step is to calculate the partial derivative for the eigenvalue equation

$$\partial_\mu H |\phi_0\rangle + H |\partial_\mu \phi_0\rangle = \partial_\mu E_0 |\phi_0\rangle + E_0 |\partial_\mu \phi_0\rangle . \quad (2.124)$$

Multiplying by $\langle \phi_n |$ (with $n \neq 0$, meaning that $\langle \phi_n | \phi_0 \rangle = \delta_{n,0} = 0$) gives:

$$\langle \phi_n | \partial_\mu H |\phi_0\rangle + \langle \phi_n | H | \partial_\mu \phi_0 \rangle = \langle \phi_n | \partial_\mu E_0 | \phi_0 \rangle + E_0 \langle \phi_n | \partial_\mu \phi_0 \rangle \quad (2.125)$$

$$\langle \phi_n | \partial_\mu H |\phi_0\rangle + E_n \langle \phi_n | \partial_\mu \phi_0 \rangle = \partial_\mu E_0 \langle \phi_n | \phi_0 \rangle + E_0 \langle \phi_n | \partial_\mu \phi_0 \rangle \quad (2.126)$$

$$\langle \phi_n | \partial_\mu H |\phi_0\rangle + E_n \langle \phi_n | \partial_\mu \phi_0 \rangle = E_0 \langle \phi_n | \partial_\mu \phi_0 \rangle . \quad (2.127)$$

This means that the term $\langle \phi_n | \partial_\mu \phi_0 \rangle$ can be expressed by the derivative of the Hamiltonian:

$$\langle \phi_n | \partial_\mu \phi_0 \rangle = \frac{\langle \phi_n | \partial_\mu H | \phi_0 \rangle}{E_n - E_0} \quad (2.128)$$

This gives the following expression for the quantum geometric tensor:

$$\mathcal{Q}_{\mu\nu} = \sum_{n \neq 0} \frac{\langle \phi_0 | \partial_\mu H | \phi_n \rangle \langle \phi_n | \partial_\nu H | \phi_0 \rangle}{(E_0 - E_n)^2} \quad (2.129)$$

For a non-degenerate Bloch eigenstate $|\psi_n(\mathbf{k})\rangle$ with crystal momentum \mathbf{k} and band index n , the quantum geometric tensor is

$$\mathcal{Q}_{ij}^n = \sum_{m \neq n} \frac{\langle \psi_n | \partial_{k_i} H(\mathbf{k}) | \psi_m \rangle \langle \psi_m | \partial_{k_j} H(\mathbf{k}) | \psi_n \rangle}{(E_m - E_n)^2} \quad (2.130)$$

Quantum Metric and Superfluid Weight

The quantum metric became of interest in the context of flat-band superconductivity. From single-band BCS theory, the superfluid weight depends just on the derivative of the band

$$D_{S,ij} = \frac{e^2}{\hbar^2} \int \frac{d^d k}{(2\pi)^d} f(\epsilon(\mathbf{k})) \frac{\partial^2 \epsilon(\mathbf{k})}{\partial k_i \partial k_j}, \quad (2.131)$$

which is zero for a flat band. On the other hand, $T_C \propto e^{-1/n_F U}$ with the density of states at the fermi level n_F so that for a flat band, the critical temperature is exponentially enhanced. So even though BCS theory predicts pairing, there is no superconductivity with just the single-band superfluid weight.

Peotta and Törmä showed that in multi-band system, there is an additional contribution to the superfluid weight [26]:

$$D_{S,\text{geom},ij} \propto M_{ij} \quad (2.132)$$

that can be nonzero even for a flat band. M_{ij} is the quantum metric integrated over the Brillouin zone:

$$M_{ij} = \sum_{\mathbf{k}} \Re Q_{ij}^n \quad (2.133)$$

with the band index of the flat band n .

This connection is derived only in the completely flat band limit, so Liang et al. developed a general theory in the framework of linear response theory which can be used to distinguish conventional and geometric contribution [28]. The superfluid weight from this approach is:

$$D_{\mu\nu}^S = \sum_{\mathbf{k}} \sum_{m,n,p,q} C_{pq}^{mn} [j_{\mu,\uparrow}(\mathbf{k})]_{mn} [j_{\nu,\downarrow}(-\mathbf{k})]_{qp} \quad (2.134)$$

$$C_{pq}^{mn} = 2 \sum_{i,j} \frac{n(E_i) - n(E_j)}{E_j - E_i} w_{+,im}^* w_{+,jn} w_{-,jp}^* w_{-,iq}, \quad (2.135)$$

Make notation coherent with my BCS notation for non-interacting H

where the E_i are the eigenvalues of the BdG Hamiltonian, so $i \in \{1, \dots, 2f\}$ with the number of bands f . The current operator is

$$[j_{\mu,\sigma}(\mathbf{k})]_{mn} = \langle m | \partial_{\mu} H_{\sigma}(\mathbf{k}) | n \rangle_{\sigma}, \quad (2.136)$$

with $|m\rangle$ being the eigenvectors of the non-interacting Hamiltonian H , the Bloch functions. The w terms are the elements of the unitary matrix $U_{\mathbf{k}}$ that diagonalizes the BdG Hamiltonian eq. (2.55):

$$U_{\mathbf{k}} = \begin{pmatrix} w_{+,11} & w_{+,21} & \cdots & w_{+,2,f1} \\ w_{+,12} & w_{+,22} & \cdots & w_{+,2,f2} \\ \vdots & \vdots & \ddots & \vdots \\ w_{+,1f} & w_{+,2f} & \cdots & w_{+,2,ff} \\ w_{-,11} & w_{-,21} & \cdots & w_{-,2,f1} \\ w_{-,12} & w_{-,22} & \cdots & w_{-,2,f2} \\ \vdots & \vdots & \ddots & \vdots \\ w_{-,1f} & w_{-,2f} & \cdots & w_{-,2,ff} \end{pmatrix} \quad (2.137)$$

Equation (2.134) splits up into two parts:

$$D_{\mu\nu}^S = D_{\text{conv},\mu\nu}^S + D_{\text{geom},\mu\nu}^S \quad (2.138)$$

where the geometric term $D_{\text{geom},\mu\nu}^S$ is the term that only depends on the off-diagonal elements of the current operator:

$$D_{\text{geom},\mu\nu}^S = \sum_{\mathbf{k}} \sum_{m \neq n, p \neq q} C_{pq}^{mn} [j_{\mu,\uparrow}(\mathbf{k})]_{mn} [j_{\nu,\downarrow}(-\mathbf{k})]_{qp} \quad (2.139)$$

The formula eq. (2.134) will be used in this thesis to compare with the results from the FMP method.

To understand this connection between the superfluid weight and the quantum metric, the concept of Wannier functions is needed. They are the Fourier transform of the Bloch functions, so while Bloch functions are localized in energy, Wannier functions are localized in space [70]. Wannier functions are used to characterize electronic orbitals in solids, most commonly in the form of maximally localized Wannier functions [71]. They have two important properties: the center of the Wannier function showing the center of the electronic orbital and the spread showing how localized the maximally localized Wannier functions are.

A flat-band system can be described by an effective spin Hamiltonian in which the exchange coupling (and in the superfluid weight) is controlled by

the overlap of the Wannier functions [72]. Because the spread of the Wannier functions is bounded from below by the trace of the integrated quantum metric

$$M_{ij} = \sum_k \Re Q_{ij}^n, \quad (2.140)$$

this connects the superfluid weight and the quantum metric as in eq. (2.132).

In magic angle twisted bilayer graphene, one of the prime example for a flat band system supporting superconductivity it has recently been measured that the superfluid weight cannot be explained by the conventional contributions alone and it is instead carried by geometric contributions [29].

3

Decorated Graphene Model

Following the 2018 discovery of superconductivity in twisted bilayer graphene [24], graphene-based systems gained a renewed interest as a platform for strongly correlated physics. Two methods to engineer strong electron correlations emerged: twisted multilayer systems [[andreibgrapheneBilayersTwist2020](#), 24, 29, 73, 74] and multilayer systems without twisting, such as Bernal bilayer, ABC or ABCA layered systems [25]. Through different means, electrons in these systems become localized so that interaction effects get more strongly pronounced. Connecting both kind of systems is the strong quantum geometry coming from the graphene Dirac cones [27], which plays a role in stabilizing superconducting [28, 29] and magnetic order [30, 31].

Witt et al. suggested another platform for strongly correlated physics based on graphene with the same strong quantum geometry, but higher intrinsic energy scales and thus also higher critical temperatures for strong correlation phenomena [75]. The model is inspired by an earlier experiment [76] of a SiC(0001) substrate with a single layer of graphene on top and Sn as an intercalant¹ between the substrate and the graphene layer. The system shows signs of Mott-Hubbard bands, a hallmark of strong correlation physics. Witt et al. suggested that by using different group-IV intercalants (C, Si, Ge, Sn, Pb) between the graphene sheet and the semiconducting SiC(0001) substrate, different distances to the graphene sheet occur in the ground state. Band structures obtained from Density Functional Theory (DFT) show a relatively flat band at the Fermi level from the intercalant's p_z orbitals hybridized to the Dirac bands of graphene for all intercalants, with the hybridization strength being tuned by the equilibrium distance of the graphene sheet and the intercalants.

In this thesis I will be treating an elemental model introduced in the work by Witt et al. capturing the essential flat band character of the system. The lattice structure can be seen in fig. 3.1. It consists of the usual hexagonal graphene lattice, with an additional atom at one of the sublattice sites providing the flat band. Here, the hopping V models the hybridization

¹An intercalant is an atom or molecule inserted between the layers of layered system.

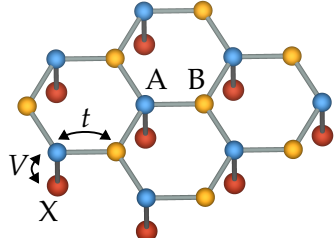


Figure 3.1 – Lattice structure of decorated graphene honeycomb lattice. with impurity X hybridized to sublattice site A. There is only hopping t between sublattices A and B as well as V between X and A atoms. Created using VESTA [77].

This elemental model shows two symmetry distinct Mott states for the small and large V regimes: in the low V regime, the X are responsible for the development of local moments and Mottness occurs at, where in the high V limit, the B atom are responsible. Between these Mott states emerges a metallic state, similar to the topological phase transition of non-interacting bands in the Su-Schrieffer-Heeger model [78].

In twisted or untwisted multilayer graphene systems, the energy scale for the emergence of ordered phases is $\mathcal{O}(\text{meV})$, corresponding to temperatures of a few K [21, 79]. In contrast, the energy scale in this decorated graphene model is set by the hopping t , i.e. $\mathcal{O}(\text{eV})$ for graphene, so that the correlated flat band physics might persist to higher temperatures.

3.1 Lattice Structure

Monolayer graphene forms a honeycomb lattice [[yangStructuregrapheneIts2018](#)], which is a hexagonal Bravais lattice with a two-atom basis, as can be seen in fig. 3.2a. The primitive lattice vectors of the hexagonal lattice are:

$$\mathbf{a}_1 = \frac{a}{2} \begin{pmatrix} 1 \\ \sqrt{3} \end{pmatrix}, \quad \mathbf{a}_2 = \frac{a}{2} \begin{pmatrix} 1 \\ -\sqrt{3} \end{pmatrix} \quad (3.1)$$

with lattice constant $a = \sqrt{3}a_0 \approx 2.46 \text{ \AA}$, using the nearest-neighbor distance a_0 . The vectors from atom A to the nearest-neighbor atoms B_i ($i = 1, 2, 3$) are

$$\delta_{AB,1} = \begin{pmatrix} 0 \\ \frac{a}{\sqrt{3}} \end{pmatrix}, \quad \delta_{AB,2} = \begin{pmatrix} \frac{a}{2} \\ -\frac{a}{2\sqrt{3}} \end{pmatrix}, \quad \delta_{AB,3} = \begin{pmatrix} -\frac{a}{2} \\ -\frac{a}{2\sqrt{3}} \end{pmatrix} \quad (3.2)$$

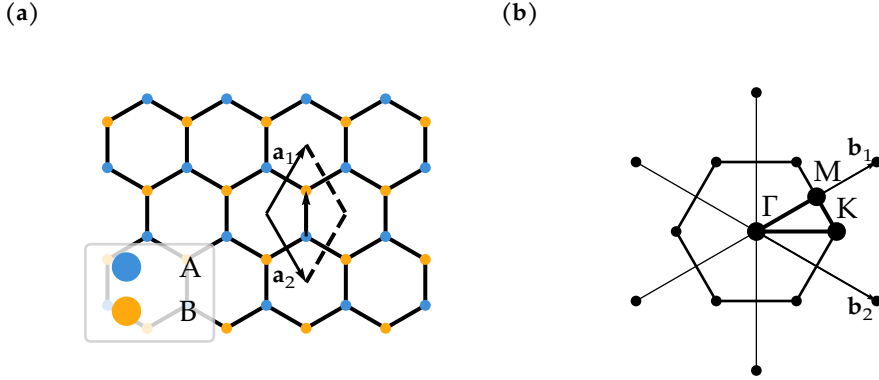


Figure 3.2 – Graphene lattice structure and Brillouin zone. (a) graphene lattice structure with primitive lattice vectors $\mathbf{a}_1, \mathbf{a}_2$ and (b) Brillouin zone with reciprocal vectors $\mathbf{b}_1, \mathbf{b}_2$. Both images created with lattpy [80].

and the vectors from atom B to the nearest-neighbor atoms A_i ($i = 1, 2, 3,$) are

$$\delta_{BA,1} = \begin{pmatrix} 0 \\ -\frac{a}{\sqrt{3}} \end{pmatrix}, \quad \delta_{BA,2} = \begin{pmatrix} -\frac{a}{2} \\ \frac{a}{2\sqrt{3}} \end{pmatrix}, \quad \delta_{BA,3} = \begin{pmatrix} \frac{a}{2} \\ \frac{a}{2\sqrt{3}} \end{pmatrix}. \quad (3.3)$$

The primitive reciprocal lattice vectors $\mathbf{b}_1, \mathbf{b}_2$ fulfill:

$$\mathbf{a}_1 \cdot \mathbf{b}_1 = \mathbf{a}_2 \cdot \mathbf{b}_2 = 2\pi \quad (3.4)$$

$$\mathbf{a}_1 \cdot \mathbf{b}_2 = \mathbf{a}_2 \cdot \mathbf{b}_1 = 0, \quad (3.5)$$

so that

$$\mathbf{b}_1 = \frac{2\pi}{a} \begin{pmatrix} 1 \\ \frac{1}{\sqrt{3}} \end{pmatrix}, \quad \mathbf{b}_2 = \frac{2\pi}{a} \begin{pmatrix} 1 \\ -\frac{1}{\sqrt{3}} \end{pmatrix}. \quad (3.6)$$

The first Brillouin zone of the hexagonal lattice is shown in fig. 3.2b, with the points of high symmetry

$$\Gamma = \begin{pmatrix} 0 \\ 0 \end{pmatrix}, \quad M = \frac{\pi}{a} \begin{pmatrix} 1 \\ \frac{1}{\sqrt{3}} \end{pmatrix}, \quad K = \frac{4\pi}{3a} \begin{pmatrix} 1 \\ 0 \end{pmatrix}. \quad (3.7)$$

The elemental model as shown in fig. 3.1 has the following kinetic terms:

$$H_0 = -t \sum_{\langle ij \rangle, \sigma} c_{i\sigma}^{(A),\dagger} c_{j\sigma}^{(B)} + V \sum_{i\sigma\sigma'} d_{i\sigma}^\dagger c_{i\sigma'}^{(A)} + \text{h.c.} \quad (3.8)$$

with

- d - operators on the X atom
- $c^{(\epsilon)}$ - operators on the graphene sites ($\epsilon = A, B$)
- t - nearest neighbor hopping between graphene sites
- V - hopping between X and graphene A sites.

Using the Fourier transformation

$$c_{i\alpha\sigma} = \frac{1}{\sqrt{N}} \sum_{\mathbf{k}} e^{i\mathbf{k}\mathbf{r}_{i\alpha}} c_{\mathbf{k}\alpha\sigma}, \quad (3.9)$$

the hopping term becomes

$$-t \sum_{\langle ij \rangle, \sigma} c_{i\sigma}^{(A),\dagger} c_{j\sigma}^{(B)} \quad (3.10)$$

$$= -t \sum_{i\delta_{AB}\sigma} c_{i\sigma}^{(A)\dagger} c_{i+\delta_{AB},\sigma}^{(B)} \quad (3.11)$$

$$= -\frac{t}{N^2} \sum_{i,\sigma} \sum_{\mathbf{k}, \mathbf{k}', \delta_{AB}} \left(e^{-i\mathbf{k}\mathbf{r}_{i\alpha}} c_{\mathbf{k}\sigma}^{(A)\dagger} \right) \left(e^{i\mathbf{k}'\mathbf{r}_{i\alpha} + \delta_{AB}} c_{\mathbf{k}'\sigma}^{(B)} \right) \quad (3.12)$$

$$= -\frac{t}{N^2} \sum_{\mathbf{k}, \mathbf{k}', \delta_{AB}, \sigma} c_{\mathbf{k}\sigma}^{(A)\dagger} c_{\mathbf{k}'\sigma}^{(B)} e^{i\mathbf{k}'\delta_{AB}} e^{i(\mathbf{k}(\delta_A - \delta_B) + \mathbf{k}'(\delta_A - \delta_B))} \sum_i e^{-i\mathbf{k}\mathbf{R}_i} e^{i\mathbf{k}'\mathbf{R}_i} \quad (3.13)$$

$$= -\frac{t}{N^2} \sum_{\mathbf{k}, \mathbf{k}', \sigma} c_{\mathbf{k}\sigma}^{(A)\dagger} c_{\mathbf{k}'\sigma}^{(B)} \sum_{\delta_{AB}} e^{i\mathbf{k}'\delta_{AB}} e^{i(\mathbf{k}(\delta_A - \delta_B) + \mathbf{k}'(\delta_A - \delta_B))} (N^2 \delta_{\mathbf{k}, \mathbf{k}'}) \quad (3.14)$$

$$= -t \sum_{\mathbf{k}, \sigma} c_{\mathbf{k}\sigma}^{(A)\dagger} c_{\mathbf{k}\sigma}^{(B)} \sum_{\delta_{AB}} e^{i(\mathbf{k}\delta_{AB} + 2k_y a)} = \sum_{\mathbf{k}, \sigma} f_{\mathbf{k}} c_{\mathbf{k}\sigma}^{(A)\dagger} c_{\mathbf{k}\sigma}^{(B)}. \quad (3.15)$$

The factor $f_{\mathbf{k}}$ can be written out explicitly using the nearest-neighbor vectors, for example

$$\mathbf{k} \cdot \delta_{AB,1} = \begin{pmatrix} k_x \\ k_y \end{pmatrix} \cdot \begin{pmatrix} 0 \\ \frac{a}{\sqrt{3}} \end{pmatrix} = \frac{1}{\sqrt{3}} k_y. \quad (3.16)$$

This gives:

$$f_{\mathbf{k}} = -t \sum_{\delta_{AB}} e^{i(\mathbf{k}\delta_{AB} + 2k_y a)} \quad (3.17)$$

$$= -te^{2ik_y a} \left(e^{\frac{i}{\sqrt{3}}k_y} + e^{\frac{i}{2\sqrt{3}}(\sqrt{3}k_x - k_y)} + e^{\frac{i}{2\sqrt{3}}(-\sqrt{3}k_x - k_y)} \right) \quad (3.18)$$

$$= -te^{2ik_y a} \left(e^{\frac{i}{\sqrt{3}}k_y} + 2e^{-\frac{i}{2\sqrt{3}}k_y} \cos\left(\frac{a}{2}k_x\right) \right). \quad (3.19)$$

Using the fact that $\delta_{BA,i} = -\delta_{AB,i}$, it follows

$$-t \sum_{\delta_{BA}} e^{i\mathbf{k}\delta_{BA}} = -t \sum_{\delta_{AB}} e^{-i\mathbf{k}\delta_{AB}} = \left(-t \sum_{\delta_{AB}} e^{i\mathbf{k}\delta_{AB}} \right)^* = f_{\mathbf{k}}^*, \quad (3.20)$$

which then gives

$$H_0 = \sum_{\mathbf{k}, \sigma} C_{\mathbf{k}\sigma}^\dagger \begin{pmatrix} 0 & f_{\mathbf{k}} & V \\ f_{\mathbf{k}}^* & 0 & 0 \\ V & 0 & 0 \end{pmatrix} C_{\mathbf{k}\sigma} \quad (3.21)$$

$$C_{\mathbf{k}\sigma} = (c_{\mathbf{k}\sigma}^{A,\dagger} \ c_{\mathbf{k}\sigma}^{B,\dagger} \ d_{\mathbf{k}\sigma}^\dagger)^T \quad (3.22)$$

For the Hamiltonian in eq. (3.8) at half-filling, there always is a zero energy eigenstate with a gap separating the other bands from the zero energy band for any finite value, as shown in fig. 3.3. For $V \rightarrow \infty$, the eigenstate is $(0 \ 1 \ 0)^T$ meaning it is completely localized at the atoms of the non-decorated sublattice B. The maximally localized Wannier function associated with this state is centered and completely peaked in the B sublattice. In the opposite case of $V \rightarrow 0^+$, the eigenstate is $(0 \ 0^+ \ f_{\mathbf{k}}/f_{\mathbf{k}})^T$ except for the nodal points where $f_{\mathbf{k}} = 0$. This means that the spectral weight of the flat band is located at the X atoms.

The orbital weight of a Bloch state $|\psi_n(\mathbf{k})\rangle$ corresponding to a band n can be calculated using

$$|w_{\mathbf{k}m}^n|^2 = |\langle \Psi_n(\mathbf{k}) | m \rangle|^2 \quad (3.23)$$

where $m \in \{\text{Gr}_A, \text{Gr}_B, X\}$ marks the orbital:

$$|\text{Gr}_A\rangle = (1 \ 0 \ 0)^T, \ |\text{Gr}_B\rangle = (0 \ 1 \ 0)^T, \ |X\rangle = (0 \ 0 \ 1)^T. \quad (3.24)$$

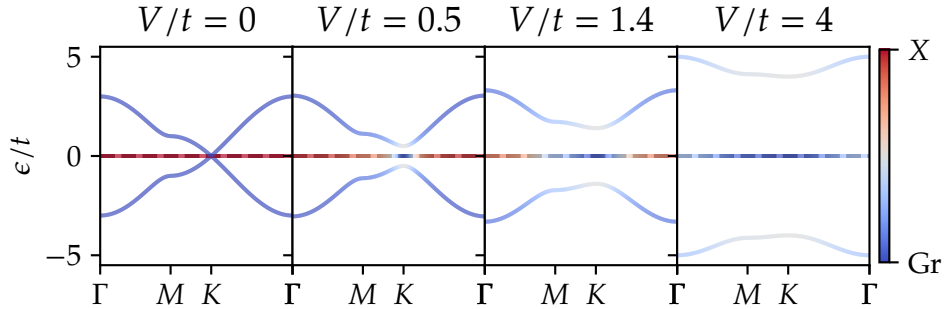


Figure 3.3 – Decorated graphene band structure. The orbital weight $W_{\mathbf{k}}$ is marked in color, showing how the flat band switches over from being of X character to being of Gr character when tuning the hybridization V .

The orbital character of the bands in fig. 3.3 is calculated via

$$W_{\mathbf{k}} = w_{\mathbf{k},X} - (w_{\mathbf{k},\text{Gr}_A} + w_{\mathbf{k},\text{Gr}_B}). \quad (3.25)$$

It shows how the flat band switches over from being completely of X character to being of Gr character.

3.2 Quantum Geometry

Between the edge cases of $V \rightarrow \infty$ and $V \rightarrow 0^+$, there is no gap closure when keeping $V > 0$, which means that the Wannier center must not have moved. Instead, the maxima of the Wannier centers shift to the three neighboring X sites. As already discussed in section 2.4, this behavior of the Wannier spread is dictated by the quantum metric. Figure 3.4 shows how the X-orbital weight of the flat band follows the integrated quantum metric

$$M = \frac{1}{N_{\mathbf{k}}} \sum_{\mathbf{k}} g_{xx}(\mathbf{k}) + g_{yy}(\mathbf{k}) \quad (3.26)$$

being finite for low V and then going to 0 for large V . This mean that following section 2.4, the model does not support superconductivity for high V because there is no geometric contribution to the superfluid weight at the flat band. For low V there will be a geometric contribution, so superconductivity can be expected in that parameter regime. The structure of localized orbitals hybridizing

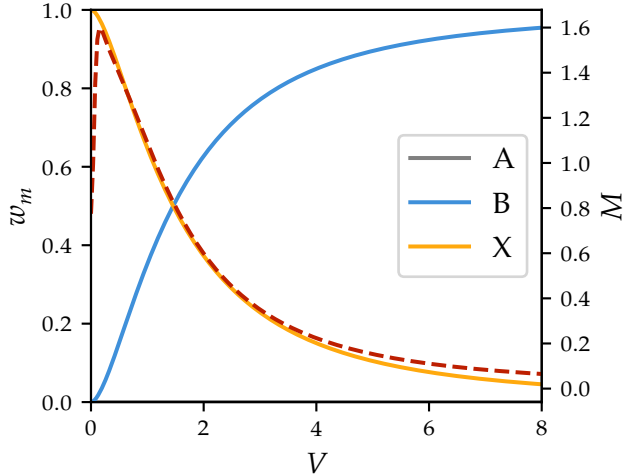


Figure 3.4 – Orbital weight of the flat band and integrated quantum metric. The orbital weight is calculated as $w_m = \sum_k |w_{km}|^2$ ($m \in \{\text{Gr}_A, \text{Gr}_B, X\}$) and the integrated quantum metric M is marked as a dotted line.

with Dirac states is similar to other strongly correlated graphene systems, such as in the heavy Fermion description of magic angle twisted bilayer graphene [81].

Application of the Finite-Momentum Pairing Method

4

Chapter 2 introduced the method of enforcing a finite momentum on the order parameter to gain access to the coherence length ξ_0 and the London penetration depth $\lambda_{L,0}$. In this chapter, it will be applied in two ways: in section 4.1 on the mean-field level as introduced in section 2.2 on the decorated graphene model, see chapter 3. Here, the influence of the quantum geometry on superconductivity as explained in section 2.4 will be explored.

In section 4.2, it is applied to the one-band Hubbard model on a square lattice, both on the mean-field level and using DMFT as introduced in section 2.3. DMFT gives the opportunity to explore the BCS-BEC crossover phenomenon and the simpler model is an opportunity to compare the results from DMFT and BCS theory.

4.1 BCS: Decorated graphene Model

In BCS theory, the method involves self-consistently solving the gap equation for a set of external parameters, which in the case of the decorated graphene model are the Hubbard interaction U , the hybridization V as well as temperature T and Cooper pair momentum \mathbf{q} . This gives gap values Δ_α for the three orbitals $\alpha \in \{\text{Gr}_A, \text{Gr}_B, X\}$.

Critical Temperatures

The zero-temperature lengths $\xi_0, \lambda_{L,0}$ are extracted from the temperature dependence $\xi(T), \lambda_L(T)$, for example

$$\xi(T) = \xi_0 \left(1 - \frac{T}{T_C}\right)^{-\frac{1}{2}}. \quad (4.1)$$

This means the first step in the analysis is to find the critical temperature T_C . Finding T_C directly by

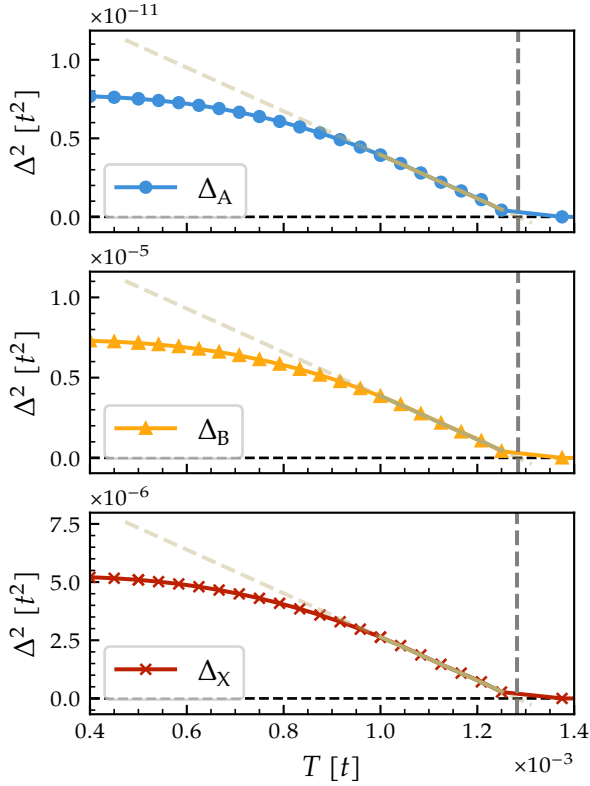


Figure 4.1 – Extraction of T_C from the linear behavior of the order parameter. Shown is the square of the gap Δ_α near T_C for $U = 0.01t$ and $V = 1.6t$. The linear fit for extracting T_C is shown in tan, the corresponding T_C is marked by the dashed gray line.

Instead, it can be extracted from the linear behavior of the order parameter near T_C , see eq. (2.9):

$$|\Delta_\alpha|^2 \propto T_C - T. \quad (4.2)$$

For a specific U and V , this is shown in fig. 4.1. Notable here is that even though Δ_A is order of magnitude smaller than Δ_B and Δ_X , T_C is the same for every orbital.

Figure 4.2 shows the extracted T_C and gaps against the hybridization V . T_C follows the maximal value of the Δ_α , switching over from X to Gr_B at $V = 1.44t$. The value of Δ_α exactly follows the orbital weight w_α of the flat band, for the orbitals $\alpha \in \{\text{Gr}_A, \text{Gr}_B, X\}$. In contrast to a repulsive Hubbard interaction [75] there is no gap closure for a medium V , instead there is just a minimum of the maximal gap value.

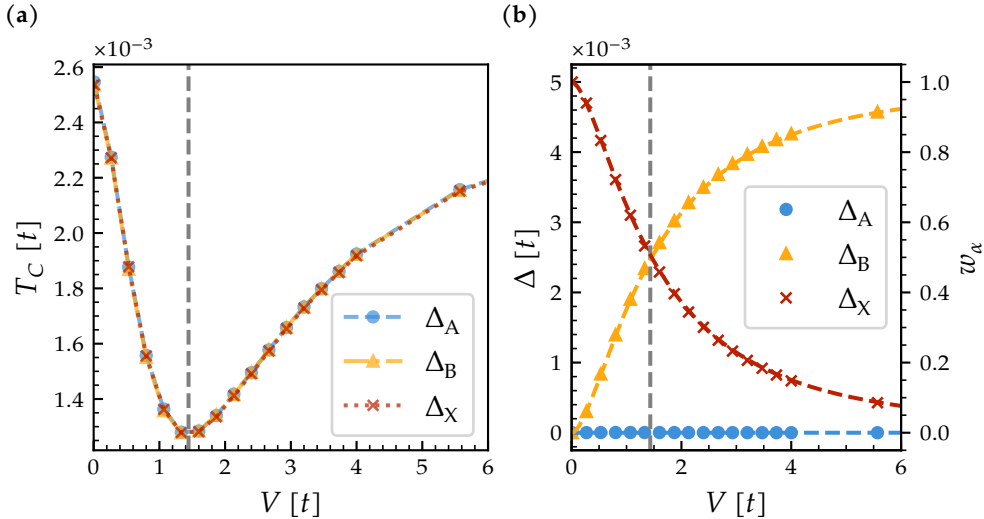


Figure 4.2 – Critical temperatures and gaps against V . (a) T_C against hybridization V , the same for all three orbitals. (b) Gaps Δ_α for the same values of V . The dashed lines are the orbital weight of the flat band as defined in section 3.2. The dashed value $V = 1.44t$ is taken from the minimum of $T_C(V)$, coinciding with the switchover of the orbital character. Both plots are for the same $U = 0.01t$.

Extracting the Superconducting Length Scales

The correlation length $\xi(T)$ is associated with the breakdown of the order parameter:

$$|\Psi_{\mathbf{q}}|^2 = |\Psi_0|^2 (1 - \xi(T)^2 q^2) , \quad (4.3)$$

which means that the q_C where the order parameter breaks down is related to the correlation length via

$$\xi = \frac{1}{q_C} . \quad (4.4)$$

The momentum \mathbf{q} is chosen as $\mathbf{q} = x \cdot \mathbf{b}_1$ with the reciprocal vector \mathbf{b}_1 and $x \in [0, 0.5]$. For $x > 0.5$, the Similar to finding T_C , numerical calculations near the point where the gap goes to zero are hard to converge, so instead the

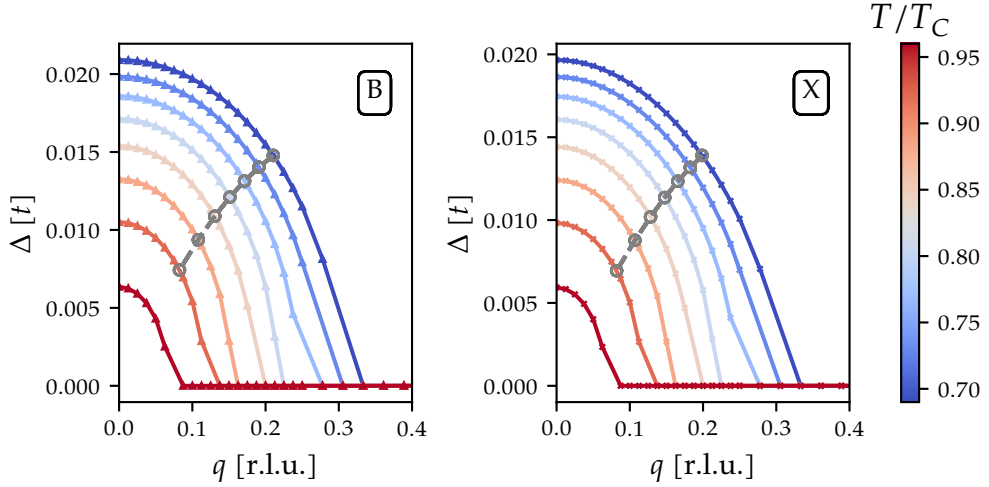


Figure 4.3 – Suppression of the order parameter with \mathbf{q} for $V = 1.5t$ and $U = 0.1t$. The x-axis is marked in relative lattice units, i.e. $\mathbf{q} = \mathbf{q} \cdot \mathbf{b}_1$ for the reciprocal unit vector \mathbf{b}_1 . Marked in gray are the points at which the gaps have fallen off to $1/\sqrt{2}$ of their value at $\mathbf{q} = 0$.

criterion employed here is to choose \mathbf{Q} such that

$$\left| \frac{\psi_{\mathbf{Q}}(T)}{\psi_0(T)} \right| = \frac{1}{\sqrt{2}}, \quad (4.5)$$

and then take

$$\xi = \frac{1}{\sqrt{2}\mathbf{Q}}, \quad (4.6)$$

compare ref. [18] for discussion about this method and comparison to other ways to extract the superconducting length scales from the \mathbf{q} -dependence of the order parameter.

As shown in fig. 4.2b, only Δ_B and Δ_X have a significant contribution in the parameter range of U here, so for these the \mathbf{q} -dependence is shown in fig. 4.3 for $V = 1.5$, so in a parameter regime switching over between dominating X and B contribution. For higher temperatures $q_C \rightarrow 0$, showing how the correlation length diverges for $T \rightarrow T_C$.

In the case of high and low V where the superconducting order is dominated by one of Δ_A, Δ_X , fig. 4.4 shows that the gap does not fully go down to 0 for

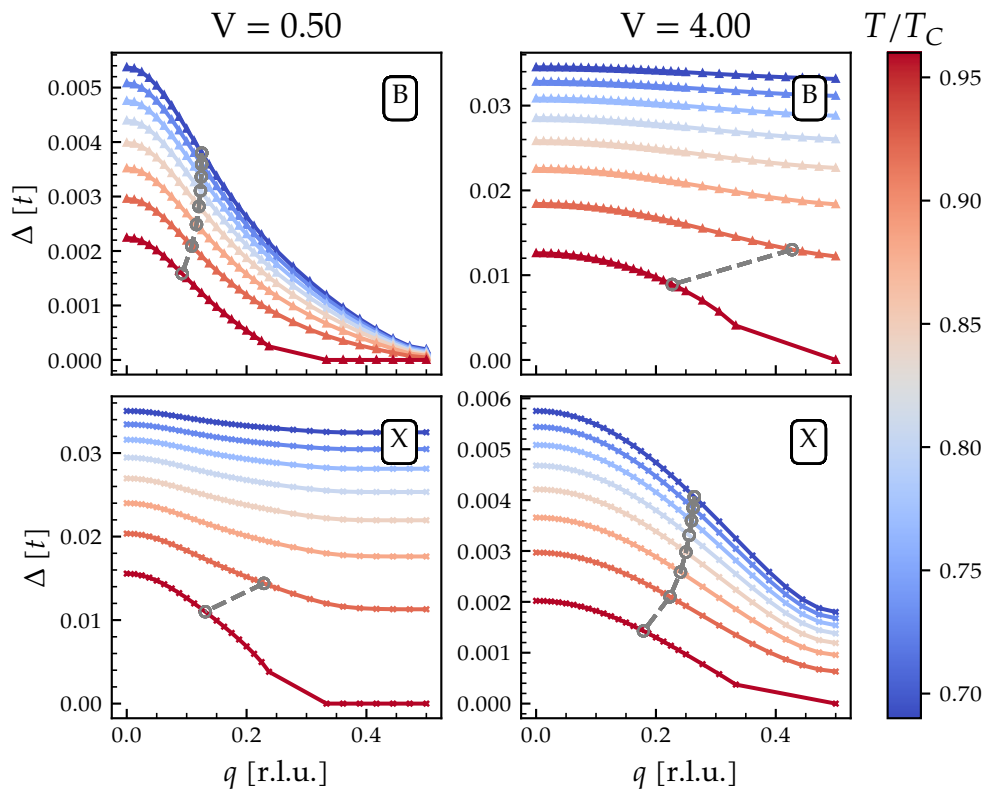


Figure 4.4 – Suppression of the order parameter with \mathbf{q} for $V = 0.5t$ and $V = 4t$ (both for $U = 0.1t$). In contrast to fig. 4.3, in this parameter regime the order parameter does not get fully suppressed for the maximal $q = 0.5$.

$\mathbf{q} = 1/2 \cdot \mathbf{b}_1$, meaning that the correlation length is smaller than

$$\xi = \frac{1}{0.5 \cdot |\mathbf{b}_1|} = \frac{\sqrt{3}a}{2\pi} = \frac{a_0}{2\pi}. \quad (4.7)$$

Besides the correlation lengths extracted from the behavior of the order parameter against \mathbf{q} , also the behavior of the superconducting current $j(\mathbf{q})$ is

Talk about limitation of GL: does not apply for high \mathbf{q}

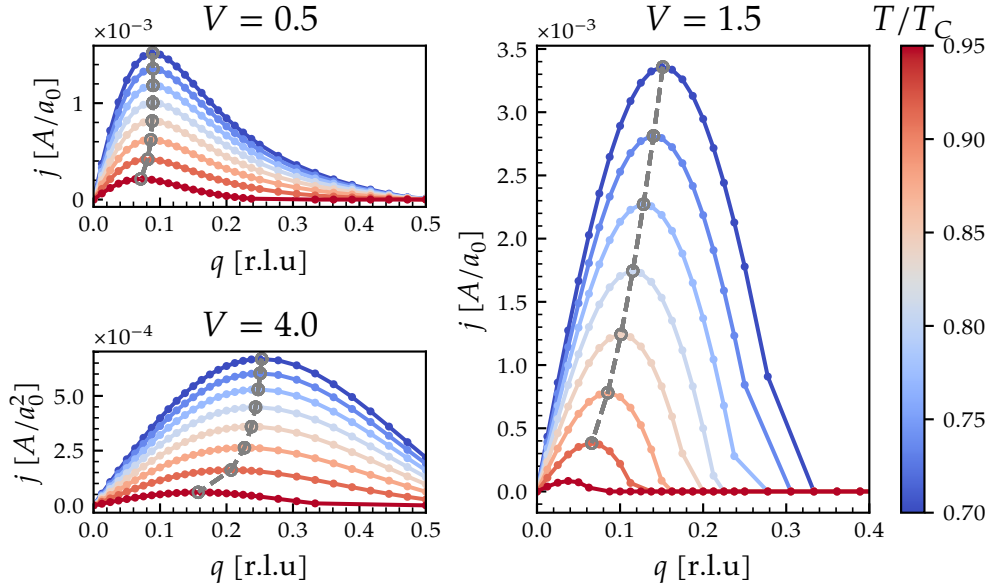


Figure 4.5 – Superconducting current from a finite \mathbf{q} . For calculation of the London penetration depth λ_L , the maximum j_{dp} of the current is needed, marked here in gray.

needed to calculate the London penetration depth λ_L via

$$\lambda_L(T) = \sqrt{\frac{\Phi_0}{3\sqrt{3}\pi\mu_0\xi(T)j_{dp}(T)}}. \quad (4.8)$$

In particular, the maximum j_{dp} (the depairing current) is used. Figure 4.5 shows the current $\mathbf{j}(\mathbf{q})$ with the maximum calculated from an interpolation marked for every temperature. As in the \mathbf{q} -dependence of the gaps, for the low and high V -values, the current is not fully suppressed for the lower temperatures and $q = 0.5$. In contrast to the analysis of the gaps, it is still possible to find a maximum of the current in these cases, but because the validity of Ginzburg-Landau theory is not given for high \mathbf{q} , it is unclear whether the connection to the superconducting length scales as derived in Ginzburg-Landau theory is given.

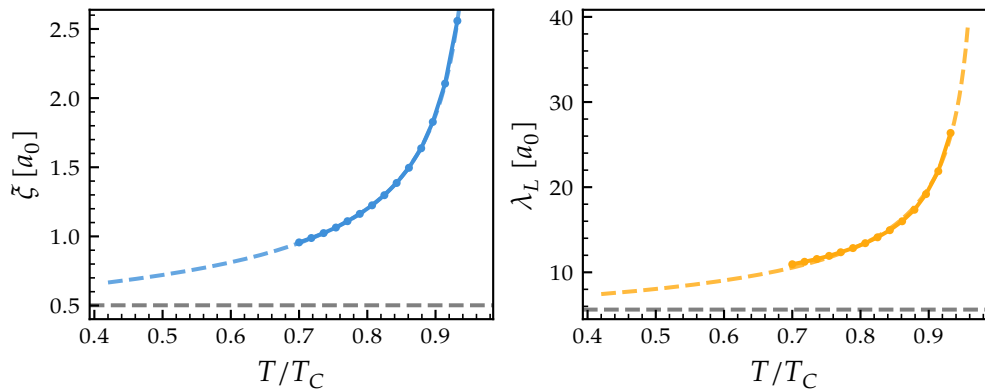


Figure 4.6 – Temperature dependence of the correlation length ξ and London penetration depth λ_L for $V = 1.50t$ and $U = 0.1t$. The fits for extracting the zero-temperature values $\xi_0, \lambda_{L,0}$ are marked as dash lines.

Figure 4.6 shows the temperature dependence for $\xi(T)$ and λ_L . These can be fit to

$$\xi(T) = \xi_0 \left(1 - \frac{T}{T_C}\right)^{-\frac{1}{2}} \quad (4.9)$$

and

$$\lambda_L(T) = \lambda_{L,0} \left(1 - \frac{T}{T_C}\right)^{-\frac{1}{2}} \quad (4.10)$$

to obtain the zero-temperature values ξ_0 and $\lambda_{L,0}$. For the low and high V (fig. 4.4): extraction of $xi(T)$ is not properly possible due to the behaviour of the gaps against q . One can try to extract information from the criterium, but the temperature dependence does not follow the fit.

Make that properly

Length Scales

Figure 4.7 shows the extracted length scales for two different values of the attractive interaction U . In the coherence length, the behavior is similar for between these two values: the orbital with the largest gap value has the shortest coherence length, with a switchover between the small and large V -values. In

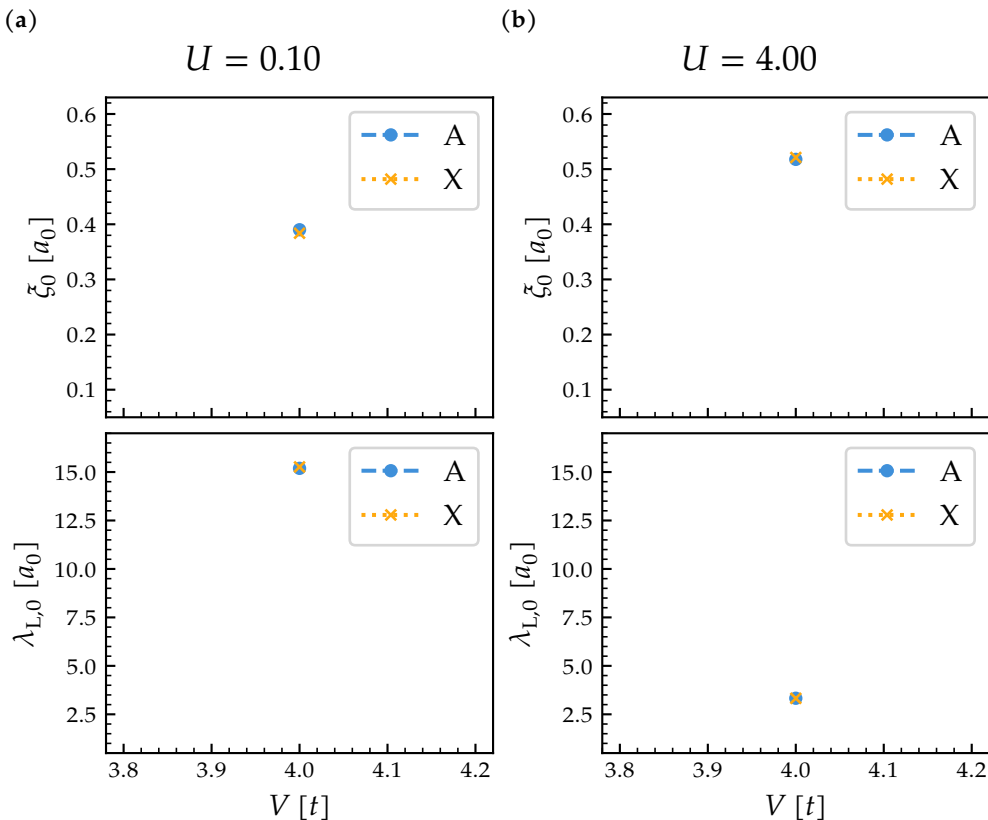


Figure 4.7 – Superconducting length scales for $U = 0.1t$. The coherence length ξ_0 is related to the size of electron pairs, the London penetration depth $\lambda_{L,0}$ is the distance magnetic fields penetrate into the material.

general, a higher attractive interaction is associated with smaller Cooper pairs. Interestingly, the orbital with vanishing gaps in the large V -limit go to the same value of ξ_0 , independent of U . It should be noted however that for the B-orbital, the coherence length becomes smaller than $\frac{a_0}{2\pi} \approx 1.6$, the minimum value that can be extracted for $V \approx 3$, so no statement about the dominating gap can be made in the large V -limit.

Talk about the exact moment of the switchover

Talk about London penetration depth

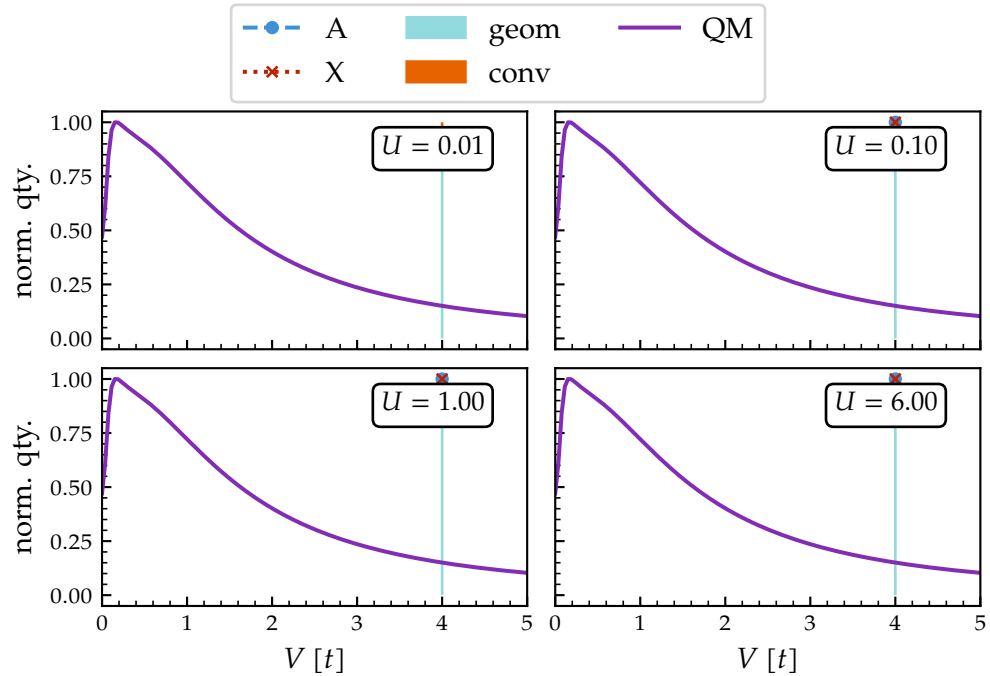


Figure 4.8 – Comparison of the superfluid weight calculated by different methods. All quantities are normalized to analyze the general trend in comparison to the quantum metric. For the calculation coming from linear response theory (see section 2.4), the geometric and conventional contributions are marked separately.

From the London penetration depth $\lambda_{L,0}$, the superfluid weight can be calculated via

$$D_S \propto \lambda_{L,0}^{-1} \quad (4.11)$$

Another way to calculate the superfluid weight from linear response theory was shown in section 2.4. Figure 4.8 shows the superfluid weight from the \mathbf{q} -dependence and the linear response formula, split up between the geometric and the conventional contribution as well as the quantum metric. The calculation from the linear response formula shows that the isolated flat band limit, where the geometric contribution dominates the superfluid weight is only given for low U , when it is on the order of the gap between the flat and dispersive bands. For $U = 1.00t$, the conventional contribution becomes bigger, while for

$U = 6.00t$ it dominates up until the gap (which is given by V) is comparable to U .

The results from the FMP method agree with the linear response insofar that they show a peak in the intermediate V -regime and go to zero for $V \rightarrow 0$ and $V \rightarrow \infty$, but the location of this peak is not the same between the two methods. Especially in the low V -limit, the FMP method (at least for this model) is at the boundary of applicability, so this is possibly a limitation of the method.

The critical temperatures in BCS theory as seen in fig. 4.2a shows a minimum in the intermediate V region. The effect of D_S that cannot be seen in the critical temperatures from BCS theory, so the expectation would be that the critical temperature actually falls off in the low and high V limit and the intermediate region is actually better for superconductivity .

Where is the maximum of q_m , compared with maximum of Aalto DS

Is that correct?

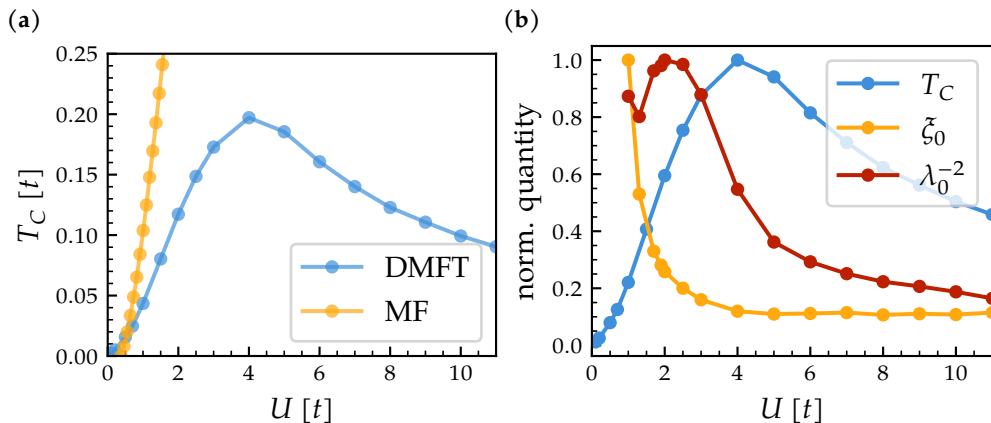


Figure 4.9 – T_C and superconducting length scales for the one-band Hubbard model. (a) T_C calculated from mean-field theory and DMFT respectively. It shows the characteristic dome of the BCS-BEC crossover that is not captured in mean-field theory. (b)

4.2 BCS and DMFT: One-Band Hubbard Model on the Square Lattice

BCS-BEC Crossover

DMFT gives insight into the phenomenon of the BCS-BEC crossover. Can extract T_C same way as above. Figure 4.9a shows T_C against U . The DMFT curve shows the typical dome-shape of the BCS-BEC crossover and the fact that the MF T_C marks the pairing temperature, which is different to the superconducting T_C .

The extraction of the superconducting length scales works the same as in section 4.1. Figure 4.9b shows how these length scales characterize the BCS-BEC crossover phenomenon: the coherence length goes to zero when going into the BEC regime, marking how the Cooper pairs become strongly localized. The superfluid weight has its maximal value for low U and also goes to zero for stronger attractive interaction,

Talk about the fact that the method works for all U values

Minimal value of coherence length?

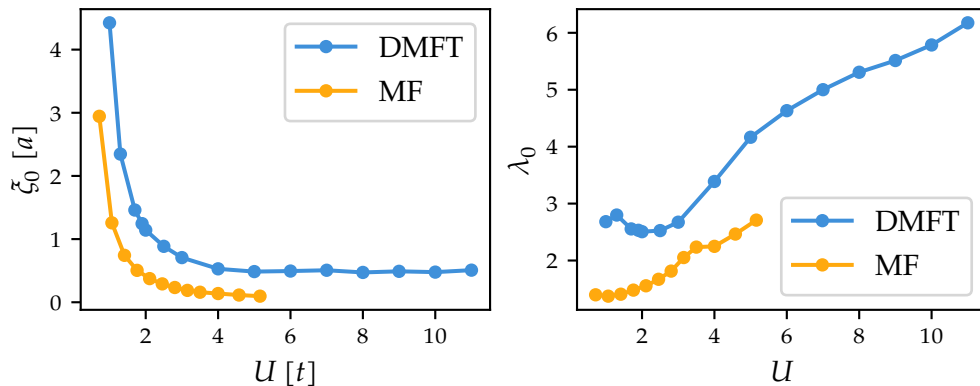


Figure 4.10 – Comparison of superconducting length scales between mean-field and DMFT.

Comparison of MF and DMFT

Figure 4.10 shows that in mean-field theory, the FMP method in BCS theory underestimates the length scales in comparison to the DMFT method.

Write what goes on in the high U limit between MF and DMFT

Why? What is captured in DMFT?

Conclusion

5

Summary

The goal of this thesis was to explore the phenomenon of superconductivity via the calculation of the coherence length and the London penetration depth, which connect to the critical temperature and the superfluid phase stiffness respectively. This was done by placing a FMP constraint on the order parameter and analyzing the suppression of the order parameter and the superconducting current.

The FMP method is based on the phenomenological Ginzburg-Landau theory, which is revised in the theoretical foundations. It is then explained how introducing a finite momentum to the order parameter gives access to the superconducting length scales. To calculate the length scales in microscopic theories, a way to introduce the finite momentum into these theories is needed. In the thesis, this is done for two theories: BCS theory and DMFT. This section also introduces the geometry of the state (characterized by the quantum metric) and how it connects to the superfluid weight, which is especially important in the context of superconductors with flat electronic bands.

One topic in superconductivity that has garnered recent interest are graphene based system that host flat bands due to their structural configuration, i.e. twisted Bilayer graphene or Bernal trilayer graphene. The next section introduces a decorated graphene model which is an approximate model for a system of group-IV intercalants between a graphene sheet and the semiconducting SiC(0001) substrate. This system also hosts flat bands and inherits the quantum geometry from the underlying graphene, which is captured by the decorated graphene model.

In the last chapter, the FMP method is used to explore the superconducting length scales. The BCS formulation is applied to the decorated graphene model, exploring how the superconductivity depends on the hybridization and how the quantum geometry of the model influence superconductivity. DMFT calculations are numerically significantly more complex and implementing it for the decorated graphene is beyond the scope of this thesis, so it is applied to a simpler model in the one band Hubbard model on a square lattice, exploring

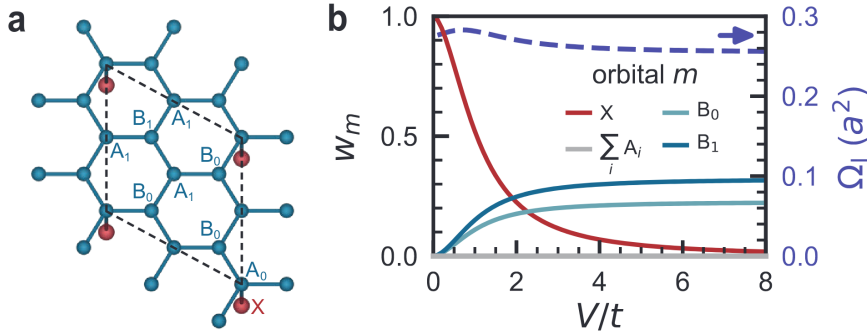


Figure 5.1 – Decorated graphene with smaller impurity density. (a) Taken from [75].

the phenomenon of the BCS-BEC crossover and seeing how the BCS and DMFT method differ.

Outlook

Starting from the mean-field results for the decorated graphene model discussed in section 4.1, further investigation into the interesting superconducting behavior with the hybridization V and why the superfluid weight does not follow the quantum metric. To this end, it is also interesting to extend mean-field treatment to the toy model with lower impurity density, see chapter 5. This model has a different $V \rightarrow \infty$ limit, retaining a finite quantum metric in this regime, which will in turn influence superconductivity.

DMFT and BCS: see whether it is a limitation of the BCS or the method in this model.

As seen in section 4.2, including the full local fluctuations with DMFT reveals physics beyond the mean-field level, so investigating the decorated graphene model in both the structure treated in this thesis and with the smaller impurity density is an interesting next step.

Split up figure

In twisted Bilayer graphene, the fact that quantum geometry is important for superconductivity in the material is well established [29]. The pairing mechanism in twisted bilayer graphene is still an open question so using the FMP method to calculate ξ_0 and $\lambda_{L,0}$ to enable a more rigorous comparison to experiment can guide in this exploration, and using the FMP method on the

mean-field level as developed in this thesis can be a tool for exploration with lower computational cost.

Bibliography

- [1] United Nations. *International Year of Quantum Science and Technology*, 2025. May 10, 2024. [URL: https://docs.un.org/A/78/L.70](https://docs.un.org/A/78/L.70) (cit. on p. 1).
- [2] He-Liang Huang et al. "Superconducting Quantum Computing: A Review". In: *Science China Information Sciences* 63.8 (2020), p. 180501. issn: 1869-1919. doi: 10.1007/s11432-020-2881-9 (cit. on p. 1).
- [3] Frank Arute et al. "Quantum Supremacy Using a Programmable Superconducting Processor". In: *Nature* 574.7779 (2019), pp. 505–510. issn: 1476-4687. doi: 10.1038/s41586-019-1666-5 (cit. on p. 1).
- [4] B. D. Josephson. "Possible New Effects in Superconductive Tunnelling". In: *Physics Letters* 1.7 (1962), pp. 251–253. issn: 0031-9163. doi: 10.1016/0031-9163(62)91369-0 (cit. on p. 1).
- [5] M. I. Faley et al. "High-Tc SQUID Biomagnetometers". In: *Superconductor Science and Technology* 30.8 (2017), p. 083001. issn: 0953-2048. doi: 10.1088/1361-6668/aa73ad (cit. on p. 1).
- [6] Alexander M. Klushin et al. "Present and Future of High-Temperature Superconductor Quantum-Based Voltage Standards". In: *IEEE Instrumentation & Measurement Magazine* 23.2 (2020), pp. 4–12. issn: 1941-0123. doi: 10.1109/MIM.2020.9062678 (cit. on p. 1).
- [7] H. Kamerlingh Onnes. "Further Experiments with Liquid Helium. G. On the Electrical Resistance of Pure Metals, Etc. VI. On the Sudden Change in the Rate at Which the Resistance of Mercury Disappears." In: *Through Measurement to Knowledge: The Selected Papers of Heike Kamerlingh Onnes 1853–1926*. Ed. by Kostas Gavroglu and Yorgos Goudaroulis. Dordrecht: Springer Netherlands, 1991, pp. 267–272. isbn: 978-94-009-2079-8. doi: 10.1007/978-94-009-2079-8_17 (cit. on p. 1).
- [8] W. Meissner and R. Ochsenfeld. "Ein neuer Effekt bei Eintritt der Supraleitfähigkeit". In: *Naturwissenschaften* 21.44 (1933), pp. 787–788. issn: 1432-1904. doi: 10.1007/BF01504252 (cit. on p. 1).
- [9] F. London. "A New Conception of Supraconductivity". In: *Nature* 140.3549 (1937), pp. 793–796. issn: 1476-4687. doi: 10.1038/140793a0 (cit. on pp. 1, 18).
- [10] J. Bardeen, L. N. Cooper, and J. R. Schrieffer. "Theory of Superconductivity". In: *Physical Review* 108.5 (1957), pp. 1175–1204. doi: 10.1103/PhysRev.108.1175 (cit. on pp. 1, 17).

- [11] Marvin L. Cohen and P. W. Anderson. "Comments on the Maximum Superconducting Transition Temperature". In: *AIP Conference Proceedings* 4.1 (1972), pp. 17–27. issn: 0094-243X. doi: 10.1063/1.2946185 (cit. on p. 1).
- [12] J. G. Bednorz and K. A. Müller. "Possible High Tc Superconductivity in the Ba–La–Cu–O System". In: *Zeitschrift für Physik B Condensed Matter* 64.2 (1986), pp. 189–193. issn: 1431-584X. doi: 10.1007/BF01303701 (cit. on p. 1).
- [13] Shin-ichi Uchida et al. "High Tc Superconductivity of La-Ba-Cu Oxides". In: *Japanese Journal of Applied Physics* 26 (1A 1987), p. L1. issn: 1347-4065. doi: 10.1143/JJAP.26.L1 (cit. on p. 1).
- [14] Niklas Witt. "Electron correlations and unconventional superconductivity in realistic solid state materials and heterostructures". Universität Hamburg (cit. on pp. 1, 4).
- [15] Qijin Chen et al. "When Superconductivity Crosses over: From BCS to BEC". In: *Reviews of Modern Physics* 96.2 (2024), p. 025002. doi: 10.1103/RevModPhys.96.025002 (cit. on p. 3).
- [16] V. J. Emery and S. A. Kivelson. "Importance of Phase Fluctuations in Superconductors with Small Superfluid Density". In: *Nature* 374.6521 (1995), pp. 434–437. issn: 1476-4687. doi: 10.1038/374434a0 (cit. on pp. 3, 8).
- [17] S. A. Kivelson. "Making High Tc Higher: A Theoretical Proposal". In: *Physica B: Condensed Matter. The Future of Materials Physics: A Festschrift for Zachary Fisk* 318.1 (2002), pp. 61–67. issn: 0921-4526. doi: 10.1016/S0921-4526(02)00775-5 (cit. on pp. 3, 8).
- [18] Niklas Witt et al. "Bypassing the Lattice BCS–BEC Crossover in Strongly Correlated Superconductors through Multiorbital Physics". In: *npj Quantum Materials* 9.1 (2024), pp. 1–10. issn: 2397-4648. doi: 10.1038/s41535-024-00706-7 (cit. on pp. 4, 8, 15, 21, 46).
- [19] Yuji Nakagawa et al. "Gate-Controlled BCS-BEC Crossover in a Two-Dimensional Superconductor". In: *Science* 372.6538 (2021), pp. 190–195. doi: 10.1126/science.abb9860 (cit. on p. 4).
- [20] Yasutomo J. Uemura. "Dynamic Superconductivity Responses in Photoexcited Optical Conductivity and Nernst Effect". In: *Physical Review Materials* 3.10 (2019), p. 104801. doi: 10.1103/PhysRevMaterials.3.104801 (cit. on p. 4).
- [21] Pierre A. Pantaleón et al. "Superconductivity and Correlated Phases in Non-Twisted Bilayer and Trilayer Graphene". In: *Nature Reviews Physics* 5.5 (2023), pp. 304–315. issn: 2522-5820. doi: 10.1038/s42254-023-00575-2 (cit. on pp. 4, 37).

-
- [22] K. S. Novoselov et al. "Electric Field Effect in Atomically Thin Carbon Films". In: *Science* 306.5696 (2004), pp. 666–669. doi: 10.1126/science.1102896 (cit. on p. 4).
 - [23] A. K. Geim and I. V. Grigorieva. "Van Der Waals Heterostructures". In: *Nature* 499.7459 (2013), pp. 419–425. issn: 1476-4687. doi: 10.1038/nature12385 (cit. on p. 5).
 - [24] Yuan Cao et al. "Unconventional Superconductivity in Magic-Angle Graphene Superlattices". In: *Nature* 556.7699 (2018), pp. 43–50. issn: 1476-4687. doi: 10.1038/nature26160 (cit. on pp. 5, 6, 36).
 - [25] Pierre A. Pantaleón et al. "Superconductivity and Correlated Phases in Non-Twisted Bilayer and Trilayer Graphene". In: *Nature Reviews Physics* 5.5 (2023), pp. 304–315. issn: 2522-5820. doi: 10.1038/s42254-023-00575-2 (cit. on pp. 5, 36).
 - [26] Sebastiano Peotta and Päivi Törmä. "Superfluidity in Topologically Nontrivial Flat Bands". In: *Nature Communications* 6.1 (2015), p. 8944. issn: 2041-1723. doi: 10.1038/ncomms9944 (cit. on pp. 5, 8, 17, 20, 33).
 - [27] T.O. Wehling, A.M. Black-Schaffer, and A.V. Balatsky. "Dirac Materials". In: *Advances in Physics* 63.1 (2014), pp. 1–76. issn: 0001-8732. doi: 10.1080/00018732.2014.927109 (cit. on pp. 5, 36).
 - [28] Long Liang et al. "Band Geometry, Berry Curvature, and Superfluid Weight". In: *Physical Review B* 95.2 (2017), p. 024515. doi: 10.1103/PhysRevB.95.024515 (cit. on pp. 5, 17, 33, 36).
 - [29] Miuko Tanaka et al. "Superfluid Stiffness of Magic-Angle Twisted Bilayer Graphene". In: *Nature* 638.8049 (2025), pp. 99–105. issn: 1476-4687. doi: 10.1038/s41586-024-08494-7 (cit. on pp. 5, 35, 36, 56).
 - [30] Ahmed Abouelkomsan, Kang Yang, and Emil J. Bergholtz. "Quantum Metric Induced Phases in Moiré Materials". In: *Physical Review Research* 5.1 (2023), p. L012015. doi: 10.1103/PhysRevResearch.5.L012015 (cit. on pp. 5, 36).
 - [31] Jianpeng Liu and Xi Dai. "Orbital Magnetic States in Moiré Graphene Systems". In: *Nature Reviews Physics* 3.5 (2021), pp. 367–382. issn: 2522-5820. doi: 10.1038/s42254-021-00297-3 (cit. on pp. 5, 36).
 - [32] B. Keimer and J. E. Moore. "The Physics of Quantum Materials". In: *Nature Physics* 13.11 (2017), pp. 1045–1055. issn: 1745-2481. doi: 10.1038/nphys4302 (cit. on p. 8).
 - [33] Piers Coleman. *Introduction to Many-Body Physics*. Cambridge University Press, Nov. 2015. isbn: 978-0-521-86488-6. doi: 10.1017/CBO9781139020916 (cit. on pp. 8, 12, 18, 24).

-
- [34] Michael Tinkham. *Introduction to Superconductivity*. 2. ed. International Series in Pure and Applied Physics. New York: McGraw-Hill, 1996. 454 pp. ISBN: 978-0-07-064878-4 (cit. on pp. 8, 16, 18).
 - [35] Henrik Bruus and Karsten Flensberg. *Many-Body Quantum Theory in Condensed Matter Physics: An Introduction*. Oxford Graduate Texts. Oxford, New York: Oxford University Press, Nov. 11, 2004. 466 pp. ISBN: 978-0-19-856633-5 (cit. on pp. 8, 24, 26).
 - [36] Anatolii Ivanovich Larkin and Andrei Andreevich Varlamov. *Theory of Fluctuations in Superconductors*. Oxford Science Publications 127. Oxford Oxford: Clarendon Press Oxford University Press, 2005. ISBN: 978-0-19-852815-9 (cit. on p. 8).
 - [37] K. H. Bennemann and John B. Ketterson, eds. *Superconductivity*. Berlin, Heidelberg: Springer Berlin Heidelberg, 2008. ISBN: 978-3-540-73252-5. doi: 10.1007/978-3-540-73253-2 (cit. on p. 8).
 - [38] Jiabin Yu et al. "Quantum Geometry in Quantum Materials". arXiv preprint (2024), doi: 10.48550/arXiv.2501.00098. (Cit. on pp. 8, 30).
 - [39] E. Noether. "Invariante Variationsprobleme". In: *Nachrichten von der Gesellschaft der Wissenschaften zu Göttingen, Mathematisch-Physikalische Klasse* 1918 (1918), pp. 235–257. url: <https://eudml.org/doc/59024> (cit. on p. 9).
 - [40] Aron Beekman, Louk Rademaker, and Jasper van Wezel. "An Introduction to Spontaneous Symmetry Breaking". In: *SciPost Physics Lecture Notes* (2019), p. 011. ISSN: 2590-1990. doi: 10.21468/SciPostPhysLectNotes.11 (cit. on p. 9).
 - [41] V. L. Ginzburg and L. D. Landau. "On the Theory of Superconductivity". In: *Zhurnal Eksperimental'noi i Teoreticheskoi Fiziki* 20 (1950). Ed. by D. ter Haar, pp. 1064–1082. doi: 10.1016/b978-0-08-010586-4.50078-x (cit. on pp. 9, 11).
 - [42] Angela Q. Chen et al. "Finite Momentum Cooper Pairing in Three-Dimensional Topological Insulator Josephson Junctions". In: *Nature Communications* 9.1 (2018), p. 3478. ISSN: 2041-1723. doi: 10.1038/s41467-018-05993-w (cit. on p. 14).
 - [43] Puhua Wan et al. "Orbital Fulde–Ferrell–Larkin–Ovchinnikov State in an Ising Superconductor". In: *Nature* 619.7968 (2023), pp. 46–51. ISSN: 1476-4687. doi: 10.1038/s41586-023-05967-z (cit. on p. 14).
 - [44] Noah F. Q. Yuan and Liang Fu. "Supercurrent Diode Effect and Finite-Momentum Superconductors". In: *Proceedings of the National Academy of Sciences* 119.15 (2022), e2119548119. doi: 10.1073/pnas.2119548119 (cit. on p. 14).

-
- [45] Jami J. Kinnunen et al. "The Fulde–Ferrell–Larkin–Ovchinnikov State for Ultracold Fermions in Lattice and Harmonic Potentials: A Review". In: *Reports on Progress in Physics* 81.4 (2018), p. 046401. issn: 0034-4885. doi: 10.1088/1361-6633/aaa4ad (cit. on p. 15).
 - [46] John Bardeen. "Critical Fields and Currents in Superconductors". In: *Reviews of Modern Physics* 34.4 (1962), pp. 667–681. doi: 10.1103/RevModPhys.34.667 (cit. on p. 16).
 - [47] Ke Xu, Peigen Cao, and James R. Heath. "Achieving the Theoretical Depairing Current Limit in Superconducting Nanomesh Films". In: *Nano Letters* 10.10 (2010), pp. 4206–4210. issn: 1530-6984. doi: 10.1021/nl102584j (cit. on p. 16).
 - [48] L. C. Hebel and C. P. Slichter. "Nuclear Relaxation in Superconducting Aluminum". In: *Physical Review* 107.3 (1957), pp. 901–902. doi: 10.1103/PhysRev.107.901 (cit. on p. 17).
 - [49] L. C. Hebel and C. P. Slichter. "Nuclear Spin Relaxation in Normal and Superconducting Aluminum". In: *Physical Review* 113.6 (1959), pp. 1504–1519. doi: 10.1103/PhysRev.113.1504 (cit. on p. 17).
 - [50] Ivar Giaever and Karl Megerle. "Study of Superconductors by Electron Tunneling". In: *Physical Review* 122.4 (1961), pp. 1101–1111. doi: 10.1103/PhysRev.122.1101 (cit. on p. 17).
 - [51] Xingjiang Zhou et al. "High-Temperature Superconductivity". In: *Nature Reviews Physics* 3.7 (2021), pp. 462–465. issn: 2522-5820. doi: 10.1038/s42254-021-00324-3 (cit. on p. 18).
 - [52] J. Hubbard and Brian Hilton Flowers. "Electron Correlations in Narrow Energy Bands". In: *Proceedings of the Royal Society of London. Series A. Mathematical and Physical Sciences* 276.1365 (1963), pp. 238–257. doi: 10.1098/rspa.1963.0204 (cit. on p. 18).
 - [53] Junjiro Kanamori. "Electron Correlation and Ferromagnetism of Transition Metals". In: *Progress of Theoretical Physics* 30.3 (1963), pp. 275–289. issn: 0033-068X. doi: 10.1143/PTP.30.275 (cit. on p. 18).
 - [54] Martin C. Gutzwiller. "Effect of Correlation on the Ferromagnetism of Transition Metals". In: *Physical Review Letters* 10.5 (1963), pp. 159–162. doi: 10.1103/PhysRevLett.10.159 (cit. on p. 18).
 - [55] Daniel P. Arovas et al. "The Hubbard Model". In: *Annual Review of Condensed Matter Physics* 13 (Volume 13, 2022 2022), pp. 239–274. issn: 1947-5454, 1947-5462. doi: 10.1146/annurev-conmatphys-031620-102024 (cit. on p. 18).

-
- [56] Mingpu Qin et al. "The Hubbard Model: A Computational Perspective". In: *Annual Review of Condensed Matter Physics* 13 (Volume 13, 2022 2022), pp. 275–302. issn: 1947-5454, 1947-5462. doi: 10.1146/annurev-conmatphys-090921-033948 (cit. on p. 18).
 - [57] R. Micnas, J. Ranninger, and S. Robaszkiewicz. "Superconductivity in Narrow-Band Systems with Local Nonretarded Attractive Interactions". In: *Reviews of Modern Physics* 62.1 (1990), pp. 113–171. doi: 10.1103/RevModPhys.62.113 (cit. on p. 19).
 - [58] D. B. McWhan, T. M. Rice, and J. P. Remeika. "Mott Transition in Cr-Doped V₂O₃". In: *Physical Review Letters* 23.24 (1969), pp. 1384–1387. issn: 0031-9007. doi: 10.1103/PhysRevLett.23.1384 (cit. on p. 24).
 - [59] M. J. Rozenberg, G. Kotliar, and X. Y. Zhang. "Mott-Hubbard Transition in Infinite Dimensions. II". In: *Physical Review B* 49.15 (1994), pp. 10181–10193. issn: 0163-1829, 1095-3795. doi: 10.1103/PhysRevB.49.10181 (cit. on p. 24).
 - [60] Eva Pavarini et al., eds. *Dynamical Mean-Field Theory of Correlated Electrons*. Schriften Des Forschungszentrums Jülich Reihe Modeling and Simulation Band/volume 12. Jülich: Forschungszentrum Jülich, Zentralbibliothek, Verlag, 2022. 1 p. isbn: 978-3-95806-619-9 (cit. on p. 24).
 - [61] Antoine Georges et al. "Dynamical Mean-Field Theory of Strongly Correlated Fermion Systems and the Limit of Infinite Dimensions". In: *Reviews of Modern Physics* 68.1 (1996), pp. 13–125. doi: 10.1103/RevModPhys.68.13 (cit. on pp. 24, 27, 29).
 - [62] Olivier Parcollet et al. "TRIQS: A Toolbox for Research on Interacting Quantum Systems". In: *Computer Physics Communications* 196 (2015), pp. 398–415. issn: 0010-4655. doi: 10.1016/j.cpc.2015.04.023 (cit. on p. 29).
 - [63] A. Amaricci et al. "EDIpak: A Parallel Exact Diagonalization Package for Quantum Impurity Problems". In: *Computer Physics Communications* 273 (2022), p. 108261. issn: 0010-4655. doi: 10.1016/j.cpc.2021.108261 (cit. on p. 29).
 - [64] Igor Krivenko. *Krivenko/Edipack2triqs*. Mar. 10, 2025. url: <https://github.com/krivenko/edipack2triqs> (cit. on p. 29).
 - [65] Michel Caffarel and Werner Krauth. "Exact Diagonalization Approach to Correlated Fermions in Infinite Dimensions: Mott Transition and Superconductivity". In: *Physical Review Letters* 72.10 (1994), pp. 1545–1548. doi: 10.1103/PhysRevLett.72.1545 (cit. on p. 29).

-
- [66] Ran Cheng. "Quantum Geometric Tensor (Fubini-Study Metric) in Simple Quantum System: A Pedagogical Introduction". arXiv preprint (2013), doi: 10.48550/arXiv.1012.1337. (Cit. on p. 30).
 - [67] K. v. Klitzing, G. Dorda, and M. Pepper. "New Method for High-Accuracy Determination of the Fine-Structure Constant Based on Quantized Hall Resistance". In: *Physical Review Letters* 45.6 (1980), pp. 494–497. doi: 10.1103/PhysRevLett.45.494 (cit. on p. 31).
 - [68] D. J. Thouless et al. "Quantized Hall Conductance in a Two-Dimensional Periodic Potential". In: *Physical Review Letters* 49.6 (1982), pp. 405–408. doi: 10.1103/PhysRevLett.49.405 (cit. on p. 31).
 - [69] J. P. Provost and G. Vallee. "Riemannian Structure on Manifolds of Quantum States". In: *Communications in Mathematical Physics* 76.3 (1980), pp. 289–301. issn: 1432-0916. doi: 10.1007/BF02193559 (cit. on p. 31).
 - [70] Nicola Marzari et al. "Maximally Localized Wannier Functions: Theory and Applications". In: *Reviews of Modern Physics* 84.4 (2012), pp. 1419–1475. doi: 10.1103/RevModPhys.84.1419 (cit. on p. 34).
 - [71] Nicola Marzari and David Vanderbilt. "Maximally Localized Generalized Wannier Functions for Composite Energy Bands". In: *Physical Review B* 56.20 (1997), pp. 12847–12865. doi: 10.1103/PhysRevB.56.12847 (cit. on p. 34).
 - [72] Murad Tovmasyan et al. "Effective Theory and Emergent $\text{SU}(2)$ Symmetry in the Flat Bands of Attractive Hubbard Models". In: *Physical Review B* 94.24 (2016), p. 245149. doi: 10.1103/PhysRevB.94.245149 (cit. on p. 35).
 - [73] Päivi Törmä, Sebastiano Peotta, and Bogdan A. Bernevig. "Superconductivity, Superfluidity and Quantum Geometry in Twisted Multilayer Systems". In: *Nature Reviews Physics* 4.8 (2022), pp. 528–542. issn: 2522-5820. doi: 10.1038/s42254-022-00466-y (cit. on p. 36).
 - [74] Fang Xie et al. "Topology-Bounded Superfluid Weight in Twisted Bilayer Graphene". In: *Physical Review Letters* 124.16 (2020), p. 167002. doi: 10.1103/PhysRevLett.124.167002 (cit. on p. 36).
 - [75] Niklas Witt et al. "Quantum Geometry and Local Moment Swapover in Correlated Graphene Heterostructures". arXiv preprint (2025), doi: 10.48550/arXiv.2503.03700. (Cit. on pp. 36, 44, 56).
 - [76] Chitran Ghosal et al. "Electronic Correlations in Epitaxial Graphene: Mott States Proximity to a Relativistic Electron Gas". arXiv preprint (2024), doi: 10.48550/arXiv.2412.01329. (Cit. on p. 36).

- [77] Koichi Momma and Fujio Izumi. "VESTA 3 for Three-Dimensional Visualization of Crystal, Volumetric and Morphology Data". In: *Journal of Applied Crystallography* 44.6 (2011), pp. 1272–1276. issn: 0021-8898. doi: 10.1107/S0021889811038970 (cit. on p. 37).
- [78] W. P. Su, J. R. Schrieffer, and A. J. Heeger. "Soliton Excitations in Polyacetylene". In: *Physical Review B* 22.4 (1980), pp. 2099–2111. doi: 10.1103/PhysRevB.22.2099 (cit. on p. 37).
- [79] Kevin P. Nuckolls and Ali Yazdani. "A Microscopic Perspective on Moiré Materials". In: *Nature Reviews Materials* 9.7 (2024), pp. 460–480. issn: 2058-8437. doi: 10.1038/s41578-024-00682-1 (cit. on p. 37).
- [80] Dylan Jones. *Lattpy*. May 2022. url: <https://github.com/dylanljones/lattpy> (cit. on p. 38).
- [81] Zhi-Da Song and B. Andrei Bernevig. "Magic-Angle Twisted Bilayer Graphene as a Topological Heavy Fermion Problem". In: *Physical Review Letters* 129.4 (2022), p. 047601. issn: 0031-9007, 1079-7114. doi: 10.1103/PhysRevLett.129.047601 (cit. on p. 42).

Not cited

- [82] Eva Y. Andrei and Allan H. MacDonald. "Graphene Bilayers with a Twist". In: *Nature Materials* 19.12 (2020), pp. 1265–1275. issn: 1476-4660. doi: 10.1038/s41563-020-00840-0.
- [83] Eviatar Bach. "Parasweep: A Template-Based Utility for Generating, Dispatching, and Post-Processing of Parameter Sweeps". In: *SoftwareX* 13 (2021), p. 100631. issn: 2352-7110. doi: 10.1016/j.softx.2020.100631.
- [84] Si Min Chan, B. Grémaud, and G. G. Batrouni. "Pairing and Superconductivity in Quasi-One-Dimensional Flat-Band Systems: Creutz and Sawtooth Lattices". In: *Physical Review B* 105.2 (2022), p. 024502. doi: 10.1103/PhysRevB.105.024502.
- [85] University of Chicago. *Annual Register*. 1893-1930., 1896. 462 pp.
- [86] Leon N Cooper and Dmitri Feldman. *BCS: 50 Years*. WORLD SCIENTIFIC, Nov. 2010. isbn: 978-981-4304-64-1. doi: 10.1142/7728.
- [87] Leon N. Cooper. "Bound Electron Pairs in a Degenerate Fermi Gas". In: *Physical Review* 104.4 (1956), pp. 1189–1190. doi: 10.1103/PhysRev.104.1189.
- [88] Yaroslav O. Halchenko et al. "DataLad: Distributed System for Joint Management of Code, Data, and Their Relationship". In: *Journal of Open Source Software* 6.63 (2021), p. 3262. issn: 2475-9066. doi: 10.21105/joss.03262.
- [89] Charles R. Harris et al. "Array Programming with NumPy". In: *Nature* 585.7825 (2020), pp. 357–362. issn: 1476-4687. doi: 10.1038/s41586-020-2649-2.
- [90] Tamaghna Hazra, Nishchhal Verma, and Mohit Randeria. "Bounds on the Superconducting Transition Temperature: Applications to Twisted Bilayer Graphene and Cold Atoms". In: *Physical Review X* 9.3 (2019), p. 031049. doi: 10.1103/PhysRevX.9.031049.
- [91] Kukka-Emilia Huhtinen. "Superconductivity and Normal State Properties in Flat Bands". Aalto University, 2023. url: <https://aaltodoc.aalto.fi/handle/123456789/119970>.
- [92] John D. Hunter. "Matplotlib: A 2D Graphics Environment". In: *Computing in Science & Engineering* 9.3 (2007), pp. 90–95. issn: 1558-366X. doi: 10.1109/MCSE.2007.55.
- [93] K.D. Irwin and G.C. Hilton. "Transition-Edge Sensors". In: *Cryogenic Particle Detection*. Ed. by Christian Enss. Berlin, Heidelberg: Springer, 2005, pp. 63–150. isbn: 978-3-540-31478-3. doi: 10.1007/10933596_3.

-
- [94] Mingu Kang et al. "Measurements of the Quantum Geometric Tensor in Solids". In: *Nature Physics* 21.1 (2025), pp. 110–117. issn: 1745-2481. doi: 10.1038/s41567-024-02678-8.
 - [95] K. Konstantopoulou et al. "Design Optimization and Evaluation of the 3 kA MgB₂ Cable at 4.3 K for the Superconducting Link Project at CERN". In: *Supercond. Sci. Technol.* 32.8 (2019), p. 085003. doi: 10.1088/1361-6668/ab13e7.
 - [96] L. D. Landau. "On the Theory of Phase Transitions". In: *Zhurnal Eksperimental'noi i Teoreticheskoi Fiziki* 7 (1937). Ed. by D. ter Haar, pp. 19–32. doi: 10.1016/B978-0-08-010586-4.50034-1.
 - [97] Sven Linzen et al. "Quantum Detection Meets Archaeology – Magnetic Prospection with SQUIDs, Highly Sensitive and Fast". In: *New Technologies for Archaeology: Multidisciplinary Investigations in Palpa and Nasca, Peru*. Ed. by Markus Reindel and Günther A. Wagner. Berlin, Heidelberg: Springer, 2009, pp. 71–85. ISBN: 978-3-540-87438-6. doi: 10.1007/978-3-540-87438-6_5.
 - [98] Wes McKinney. "Data Structures for Statistical Computing in Python". In: Python in Science Conference. Austin, Texas, 2010, pp. 56–61. doi: 10.25080/Majora-92bf1922-00a.
 - [99] Reko P. S. Penttilä, Kukka-Emilia Huhtinen, and Päivi Törmä. "Flat-Band Ratio and Quantum Metric in the Superconductivity of Modified Lieb Lattices". In: *Communications Physics* 8.1 (2025), pp. 1–10. issn: 2399-3650. doi: 10.1038/s42005-025-01964-y.
 - [100] Matthew A. Petroff. "Accessible Color Sequences for Data Visualization". arXiv preprint (2024), doi: 10.48550/arXiv.2107.02270.
 - [101] Peter A. Rinck. *Magnetic Resonance in Medicine - A Critical Introduction*. ISBN: 978-628-01-2260-1. URL: <http://www.magnetic-resonance.org/>.
 - [102] Lucio Rossi. "Particle Accelerators and Cuprate Superconductors". In: *Physica C: Superconductivity and its Applications* 614 (2023), p. 1354360. issn: 0921-4534. doi: 10.1016/j.physc.2023.1354360.
 - [103] Damian Rybicki et al. "Perspective on the Phase Diagram of Cuprate High-Temperature Superconductors". In: *Nature Communications* 7.1 (2016), p. 11413. issn: 2041-1723. doi: 10.1038/ncomms11413.
 - [104] F. Schmidt et al. "Operation Experience and Further Development of a High-Temperature Superconducting Power Cable in the Long Island Power Authority Grid". In: *Physics Procedia*. SUPERCONDUCTIVITY CENTENNIAL Conference 2011 36 (2012), pp. 1137–1144. issn: 1875-3892. doi: 10.1016/j.phpro.2012.06.190.
 - [105] The pandas development team. *Pandas-Dev/Pandas: Pandas*. Version v2.2.3. Zenodo, Sept. 20, 2024. doi: 10.5281/ZENODO.3509134.

-
- [106] Tom Timusk and Bryan Statt. "The Pseudogap in High-Temperature Superconductors: An Experimental Survey". In: *Reports on Progress in Physics* 62.1 (1999), p. 61. issn: 0034-4885. doi: 10.1088/0034-4885/62/1/002.
 - [107] Alvin Tollestrup and Ezio Todesco. "The Development of Superconducting Magnets for Use in Particle Accelerators: From the Tevatron to the LHC". In: *Reviews of Accelerator Science and Technology* 1.01 (2008), pp. 185–210.
 - [108] Pauli Virtanen et al. "SciPy 1.0: Fundamental Algorithms for Scientific Computing in Python". In: *Nature Methods* 17.3 (2020), pp. 261–272. issn: 1548-7105. doi: 10.1038/s41592-019-0686-2.
 - [109] Di Xiao, Ming-Che Chang, and Qian Niu. "Berry Phase Effects on Electronic Properties". In: *Reviews of Modern Physics* 82.3 (2010), pp. 1959–2007. doi: 10.1103/RevModPhys.82.1959.
 - [110] Gao Yang et al. "Structure of Graphene and Its Disorders: A Review". In: *Science and Technology of Advanced Materials* 19.1 (2018), pp. 613–648. issn: 1468-6996.
 - [111] Chao Yao and Yanwei Ma. "Superconducting Materials: Challenges and Opportunities for Large-Scale Applications". In: *iScience* 24.6 (2021), p. 102541. issn: 2589-0042. doi: 10.1016/j.isc.2021.102541.
 - [112] F. C. Zhang and T. M. Rice. "Effective Hamiltonian for the Superconducting Cu Oxides". In: *Physical Review B* 37.7 (1988), pp. 3759–3761. doi: 10.1103/PhysRevB.37.3759.
 - [113] Chi Zhang et al. "Recent Progress on High-Temperature Superconducting Filters". In: *Superconductivity* 2 (2022), p. 100012. issn: 2772-8307. doi: 10.1016/j.supcon.2022.100012.

Listings

List of Figures

1.1	Critical surface of a superconductor.	2
1.2	BCS-BEC crossover.	3
1.3	Uemura plot.	4
1.4	Twisted Bilayer graphene.	6
2.1	Landau free energy and Mexican hat potential.	11
2.2	Ginzburg-Landau solutions for a finite momentum q .	16
2.3	Mapping of the full lattice problem onto a single-site impurity model.	24
3.1	Lattice structure of decorated graphene honeycomb lattice.	37
3.2	Graphene lattice structure and Brillouin zone.	38
3.3	Decorated graphene band structure.	41
3.4	Orbital weight of the flat band and integrated quantum metric.	42
4.1	Extraction of T_C from the linear behavior of the order parameter.	44
4.2	Critical temperatures and gaps against V .	45
4.3	Suppression of the order parameter with \mathbf{q} for $V = 1.5t$ and $U = 0.1t$.	46
4.4	Suppression of the order parameter with \mathbf{q} for $V = 0.5t$ and $V = 4t$ (both for $U = 0.1t$).	47
4.5	Superconducting current from a finite \mathbf{q} .	48
4.6	Temperature dependence of the correlation length ξ and London penetration depth λ_L for $V = 1.50t$ and $U = 0.1t$.	49
4.7	Superconducting length scales for $U = 0.1t$.	50
4.8	Comparison of the superfluid weight calculated by different methods.	51
4.9	T_C and superconducting length scales for the one-band Hubbard model.	53
4.10	Comparison of superconducting length scales between mean-field and DMFT.	54

5.1	Decorated graphene with smaller impurity density.	56
-----	---	-----------	----

List of Acronyms

BCS Bardeen-Cooper-Schrieffer. i, ii, 1, 2, 5, 7, 8, 17, 23, 43, 55, 56

DMFT Dynamical Mean Field Theory. i, ii, 5, 7, 8, 18, 23, 24, 43, 53, 55, 56

FMP Finite Momentum Pairing. 5, 7, 34, 52, 54, 55, 56

FF Fulde–Ferrell. 15

BdG Bogoliubov-de Gennes. 20, 33, 34

ED Exact Diagonalization. 29

DFT Density Functional Theory. 36